FACULTY
OF MATHEMATICS
AND PHYSICS
Charles University

MASTER THESIS

Bc. Marián Betušiak

Effect of the laser pulse illumination on charge collection efficiency in radiation detectors

Institute of Physics of Charles University

Supervisor of the master thesis: Doc. Ing. Eduard Belas, CSc.

Study programme: Physics

Specialization: Optics and Optoelectronics

Prague 2020

I declare that I carried out this master thesis independently, and only with the cited sources, literature and other professional sources.

I understand that my work relates to the rights and obligations under the Act No. 121/2000 Coll., the Copyright Act, as amended, in particular the fact that the Charles University has the right to conclude a license agreement on the use of this work as a school work pursuant to Section 60 paragraph 1 of the Copyright Act.

In Prague 30.7.2020 signature

I would like to thank all employees and students from the Department of Optoelectronics and Magneto-Optics at the Institute of Physics of Charles University. Above all, I would like to thank my supervisor doc. Ing. Eduard Belas CSc. for his guidance and his countless advices during the measurement and writing of this thesis. I would also like to thank prof. RNDr. Roman Grill CSc.for the tremendous amount of his time spent discussing the measured data and possible detector models. Lastly but not least, I want to thank Mgr. Jindřich Pipek for advices how to use the experimental setup and for the automation of all measurements since doing them manually would take an ungodly amount of time.

Title: Effect of the laser pulse illumination on charge collection efficiency in radiation detectors

Author: Bc. Marián Betušiak

Institute: Institute of Physics of Charles University

Supervisor of the master thesis: doc. Ing. Eduard Belas, CSc.

Abstract:

The main focus of this thesis is the characterization of the charge transport in CdZnTe radiation detectors and the study of the effect of the detector illumination on charge transport. The transport properties are evaluated using Laser-induced Transient Current Technique and the Monte Carlo simulation is used for fitting the measured current waveforms. The properties of the detector prepared from semi-insulating CdZnTe single crystal with a platinum Schottky contacts were measured in the dark in the unpolarized and polarized state and under the anode and cathode continuous LED above-bandgap illumination.

Keywords: Charge generation, Charge collection, Radiation detectors

Contents

Introduction 3
1 Theory 5
1.1 Transport equations 5
1.2 Charge transport in a planar detector 6
1.2.1 Constant electric field 8
1.2.2 Linear electric field 9
1.3 Effects of charge trapping and detrapping 12
1.3.1 Approximation beyond transit time 15
1.3.2 Trap controlled mobility 18
1.4 Surface recombination 18
1.5 Charge collection efficiency 20
2 Laser-induced Transient Current Technique 21
2.1 Monte Carlo simulation 24
3 Results and discussion 26
3.1 Detector preparation 26
3.2 I-V characteristics measurement 26
3.3 L-TCT measurement in the dark 27
3.3.1 Measurement in the unpolarized detector 28
3.3.2 Measurement in the polarized detector 31
3.3.3 Dynamics of the space charge formation in the dark 33
3.3.4 The CCE in the dark 36
3.4 Continuous anode illumination 38
3.5 Continuous cathode illumination 42
4 Conclusion 45
5 Bibliography 47
6 List of Figures 49
7 List of Tables 51
8 List of Symbols and Abbreviations 52

Introduction

Radiation detectors are used for detection of electromagnetic radiation starting with infrared through visible and continuing deep in the X-ray and gamma-ray region or for the detection of ionizing particles. There are many different types of detectors, but the most common are semiconductor detectors. They directly convert incident radiation to an electric signal, unlike scintillators that convert incident radiation to lower energy electromagnetic radiation (UV, visible) and thus require the connection with photomultipliers. Application of semiconductor detectors is ranging from astronomy and particle physics to more "everyday" uses like nuclear power plant inspection, medical imaging or X-ray quality inspection.

In order to create a high-quality X-ray and gamma-ray detector, one must first choose suitable material in the first place. The main requirements for semiconductor detectors are resistivity, bandgap, high mobility-lifetime products of charge carriers and high absorption in a used part of the spectra and with that associated density and average atomic number.

To obtain a great signal-to-noise ratio the leakage current needs to be as low as possible. One way to achieve this is the "right kind" of high resistivity - more precisely high resistivity caused by the low concentration of free carriers. This type of resistivity is closely tied with the width of the bandgap – the higher the bandgap the lower the concentration of free carriers and as a bonus the lower the thermal noise. The ideal bandgap is somewhere between 1.4 -3 eV [1]. Another way of obtaining low leakage current is achieved in the reverse direction of a p-n junction often used for silicon and germanium diode detectors.

The best energy resolution is achieved only when all of the photogenerated carriers are collected at the electrodes before the carriers either recombine or they are trapped. Therefore, high carrier mobility and carrier lifetime are required.

Lastly, the higher the absorption, the smaller the detectors can get but still retain the same signal as their less absorptive counterparts. High absorption is also useful because in some cases the preparation of larger detectors is rather difficult.

Table 0.1: Selected properties of Si, Ge, CdZnTe and GaAs [1], [2]

Material	Si	Ge	CdZnTe	GaAs
Atomic number	14	32	48, 30, 52	31, 33
Density ($g.cm^{-3}$)	2.33	5.32	5.78-6.2	5.32
Bandgap (eV)	1.12	0.67	1.5	1.43
Electron mobility μ_e ($cm^2.V^{-1}.s^{-1}$)	1400	3900	1000-1100	8000
Hole mobility μ_h ($cm^2.V^{-1}.s^{-1}$)	450	1900	50-80	400
Electron-hole pair generation energy (eV)	3.6	2.96	4.64	4.2

As can be seen in Table 0.1, germanium has excellent properties (mobility, density, atomic number) for detector fabrication except for the small bandgap and its need to be cooled down to the cryogenic temperatures preventing germanium to become room-temperature detector. In terms of bandgap, silicon is a better candidate than germanium, with roughly third of the germanium mobility, it is still perfect material for visible and light X-ray detection, but as the photon energy gets higher the ability of silicon to absorb incident radiation lowers due to silicon's low density and atomic number. While GaAs has high mobility, moderate bandgap and higher density than silicon, the detector performance is significantly debased by the presence of EL2 centre, that limits the electron lifetime [3].

Since the 1960s the cadmium telluride (CdTe) and cadmium-zinc telluride (CdZnTe) are regarded as a promising material for room-temperature X-ray and gamma-ray detectors. Great effort was taken to perfect the crystals growth process, passivation of the surface and contact preparation but detector polarization still remains an immense problem. Detector polarization can be induced either by intense X-ray and γ-ray irradiation [4] or simply by applying a bias to the detector [5].

This thesis aims to characterize charge transport in CdZnTe detectors and to study the effect of the above-bandgap illumination utilizing a Laser-induced transient current technique. It can also determine how the additional carrier injection affects the detector polarization and associated charge collection efficiency.

1 Theory

1.1 Transport equations

One of the ways to describe the charge transport in a semiconductor is using continuity equation

$$\frac{\partial n}{\partial t} = \frac{1}{e}\nabla \cdot \boldsymbol{j_e} + GR_e, \tag{1.1}$$

where n is the concentration of electrons in a conduction band, e is the elementary charge, $\mathbf{j_e}$ is the electron current density and GR_e describes the generation and recombination of the electrons. Current density is defined by drift-diffusion equation [6]

$$\boldsymbol{j_e} = en\mu_e \boldsymbol{E} + eD_e \nabla n + eS_e \nabla T, \tag{1.2}$$

where μ_e is electron mobility, $\boldsymbol{E}$ is the intensity of the applied electric field, T is absolute thermodynamic temperature, D_e is the diffusion coefficient given by equation (1.3) and S_e is the Soret coefficient given by equation (1.4).

$$D_e = \frac{k_B T}{e}\mu_e \tag{1.3}$$

$$S_e = \frac{k_B}{e} n\mu_e \tag{1.4}$$

The first term of equation (1.2) corresponds to the drift in electric field **E**, while second term is the result of diffusion. The third term describes electron transport due to the gradient of temperature in the material.

Combining equations (1.1) and (1.2) and assuming constant temperature and carrier mobility we get transport equation for electrons

$$\frac{\partial n}{\partial t} = \mu_e \boldsymbol{E}.\nabla n + \mu_e n \frac{\rho}{\varepsilon} + D_e \nabla^2 n + GR_e, \tag{1.5}$$

where the differential form of Gauss law [7] was used, ρ is the space charge density in the detector and ε is the permittivity of the material. Similarly, transport equation for holes can be obtained by switching $e \to -e$ and $\mu_e \to -\mu_h$.

1.2 Charge transport in a planar detector

The geometry of the planar detector is shown in Fig. 1.1. Assuming that the lateral dimensions of the detector are much larger than its width L, calculations can be reduced from three spatial dimensions to only one. The detector is illuminated at the centre of the electrode and laser spot with area S is small enough that the inhomogeneity of the electric field near the edges of the detector can be neglected. We also assume that the applied electric field E_0 is constant with respect to time or at least that its change during the charge carrier transit is negligible and that the photogenerated charge does not affect the local electric field. In case of strong absorption, irradiation generates electron-hole pairs just under the cathode and they are immediately separated by the electric field. Electrons are drifting towards the anode in the positive direction of the z-axis, and holes are almost immediately collected at the cathode. Some detectors may have a guard ring structure (GR in Fig. 1.1) separated by the resistive layer from the central electrode, to suppress the surface leakage current.

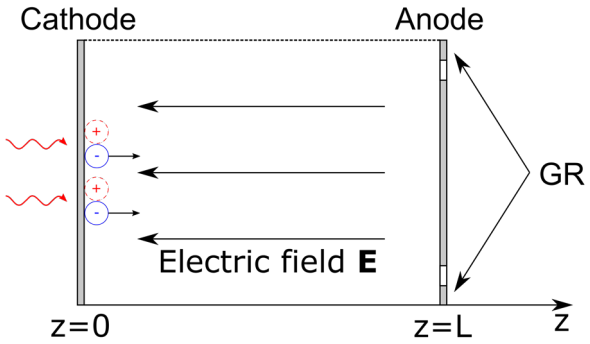

Fig. 1.1: Simplified geometry of the detector.

Internal electric field $\boldsymbol{E}(\boldsymbol{r},t)$ consisting of the applied electric field $\boldsymbol{E_0}(t)$ and the electric field induced by space charge $\boldsymbol{E_\rho}(\boldsymbol{r},t)$, can be rewritten as

$$\boldsymbol{E}(\boldsymbol{r},t) = \boldsymbol{E_0}(t) + \boldsymbol{E_\rho}(\boldsymbol{r},t) = \frac{U}{L}\boldsymbol{z} + E_\rho(z)\boldsymbol{z}, \tag{1.6}$$

where U is applied bias and $\boldsymbol{z}$ is a unit vector in the z-direction. Subsequently, the equation (1.5) transforms to

$$\frac{\partial n(z,t)}{\partial t} = \mu_e\left(\frac{U}{L} + E_\rho(z)\right)\frac{\partial n(z,t)}{\partial z} + \\ + \frac{\rho(z)}{\varepsilon}n(z,t) + D_e\frac{\partial^2 n(z,t)}{\partial z^2} + GR(z,t). \tag{1.7}$$

Knowing the concentration of the electrons, the Shockley-Ramo theorem [8] is used to obtain the shape of the current waveform. In the case of two planar electrodes, the current induced by the charge q moving with the drift velocity v is simply given by

$$I_q(t) = \frac{qv(t)}{L}. \tag{1.8}$$

The electric current induced by the electron distribution $n(z,t)$ is then described by

$$I_n(t) = -\frac{eS}{L}\int_0^L n(z,t)v_e(z)dz = \frac{\mu_e e}{L}\int_0^L n(z,t)E(z)dz, \tag{1.9}$$

which in the case of sharply localized electron cloud or constant electric field can be simplified to

$$I_n(t) = \frac{Q_0(t)v_e(t)}{L}, \tag{1.10}$$

where Q_0 is the overall moving charge and v_e is the electron drift velocity.

Photogeneration of the carriers provided by a laser pulse is defined by the generation recombination term GR in equation (1.7). Assuming the attenuation of the square laser pulse is described by the Lambert-Beer law, the generation term is then

$$GR(z,t) = \frac{N_0}{S}\frac{\alpha}{1-exp(-\alpha L)}exp(-\alpha z)\frac{1}{t_{laser}}\chi(t,0,t_{laser}), \tag{1.11}$$

where N_0 is the overall number of photogenerated carriers, S is illuminated area, α is the absorption coefficient and t_{laser} is the duration of the laser pulse and $\chi(t,0,t_{laser})$ is the boxcar function, that is equal to 1 if $0 \leq t \leq t_{laser}$ and in all other cases is equal to 0. Both fractions in the formula (1.11) are just normalizing terms of the respective distribution. However, using the GR in the computation leads to quite complicated and intricate solutions, that is why in the text below the sharply localized electron cloud $n(z,0) = \frac{N_0}{S}\delta(z)$ will often be used as an initial condition instead. This simplification is, in fact, correct since the laser pulse width has to be short enough (significantly shorter than current waveform) not to distort the current waveform, essentially becoming the Dirac delta function in time $\delta(t)$. Therefore, the term GR can be excluded and the initial condition

$$n(z,0) = \frac{N_0}{S}\frac{\alpha}{1-exp(-\alpha L)}exp(-\alpha z) \tag{1.12}$$

can be used. For high absorption coefficient (above bandgap illumination) incident light is absorbed in the thin region beneath the surface $\left(\sim\frac{1}{\alpha}\right)$, thereupon the spatial

dependence of initial carrier distribution can be disregarded and again Dirac delta-function $\delta(z)$ can be used.

1.2.1 Constant electric field

Assuming a constant electric field ($\rho = 0$), no diffusion ($D_e = 0$) and no generation or recombination of the carries, equation (1.7) takes on a simple form

$$\frac{\partial n(z,t)}{\partial t} = \mu_e E_0 \frac{\partial n(z,t)}{\partial z} \tag{1.13}$$

The solution of the transport equation (1.13) with initial condition $n(x,0) = n_0(x)$ is

$$n(z,t) = n_0(z - v_0 t), \tag{1.14}$$

where v_0 denotes drift velocity of electrons $v_0 = -\mu_e E_0$. Since the finite width of the detector is introduced only by the Schockley-Ramo theorem (equations (1.9) and (1.10)), solution (1.14) represents the initial electron distribution drifting endlessly with the velocity v.

The shape of the current waveform given by (1.10) is not affected by initial carrier distribution (assuming all carriers are generated at the same time) until the time the first electron reaches the anode and overall moving charge in the detector Q_0 starts to decrease. The time it takes charge carrier to pass the width of the detector L is called the default transit time t_{r0} and is defined as

$$t_{r0} = \frac{L}{|v_0|} = \frac{L^2}{\mu_e |U|} \tag{1.15}$$

For simplification let's assume initial spatial distribution of electrons to be Dirac delta function $n_0(x) = -\frac{Q_0}{eS}\delta(x)$, the current waveform is then described by

$$I(t) = \frac{Q_0 v_0}{L}\chi(t, 0, t_{r0}) = \frac{Q_0}{t_{r0}}\chi(t, 0, t_{r0}). \tag{1.16}$$

The boxcar function has appeared due to the electron collection at the anode. The current waveforms for different drift velocities (different biases) are shown in Fig. 1.2.

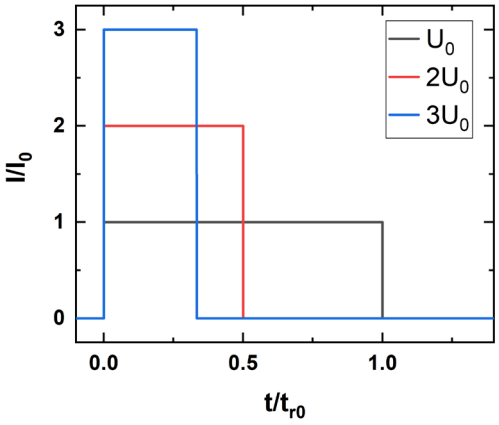

Fig. 1.2: Normalized current waveforms for different biases. Waveforms are normalized with respect to the current I_0 and trasit time t_{r0} of the U_0 waveform.

1.2.2Linear electric field

Let's assume a homogeneously charged detector. The electric field exerted by the constant space charge ρ can be easily calculated using Gauss law and is given by

$$E_\rho(z) = \frac{\rho}{\varepsilon} z - \frac{\rho L}{2\varepsilon}. \tag{1.17}$$

In some cases this electric field E_ρ can completely screen out the applied electric field E_0 and the inactive layer is formed and space charge in this region then dissipates [9]. Assuming that the electric field in the inactive layer is zero, the electric field in the detector is then

$$E(z) = E_0\, max\left(1 + \frac{\rho}{\rho_m}\left(2\frac{z}{L} - 1\right), 0\right). \tag{1.18}$$

where $\rho_m = \frac{2\varepsilon E_0}{L}$ is the space charge density for which the electric field beneath the cathode $E(0)$ is equal to zero. Formula (1.18) is also valid for the opposite electrode configuration. As can be seen in Fig. 1.3a) electric field is nonzero in the whole detector for $-|\rho_m| < \rho < |\rho_m|$, in all other cases an inactive layer with the width of $w = \frac{L}{2}\left(1 - \frac{\rho_m}{\rho}\right)$ is formed. Corresponding space charge is shown Fig. 1.3b). Since the electric field in the inactive layer is zero, electron-hole pairs generated in this layer cannot drift and recombine.

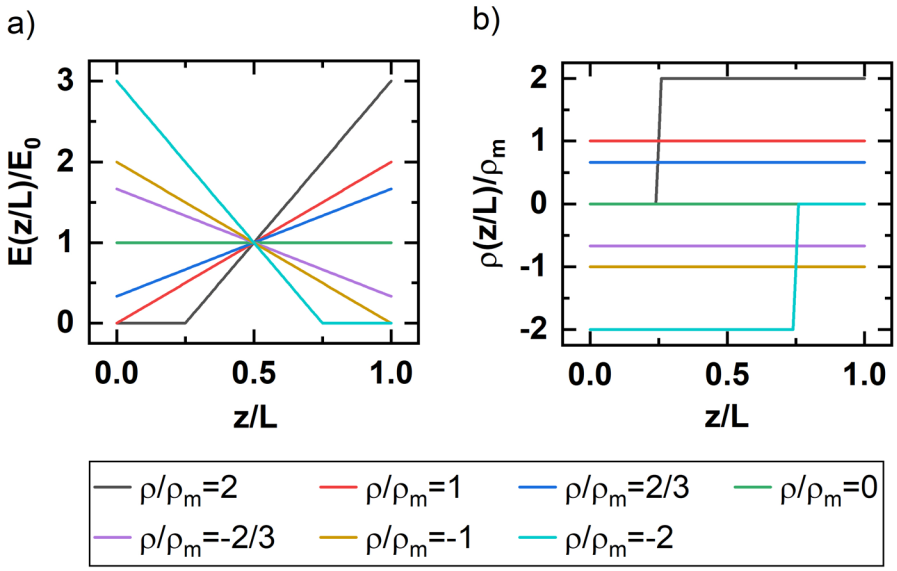

Fig. 1.3: a) Normalized electric field profile for different values of charge density ρ and b) corresponding profile of the normalized charge density.

The equation (1.7) can be rewritten for the case of the linear electric field by disregarding the diffusion and generation (recombination) of the charge carriers and substituting the formula (1.18) for the electric field E_ρ. Obtained equation is then given by

$$\frac{\partial n(z,t)}{\partial t} = \mu_e \left(E_0 + \frac{\rho}{\varepsilon} z - \frac{\rho L}{2\varepsilon}\right) \frac{\partial n(z,t)}{\partial z} + \mu_e \frac{\rho}{\varepsilon} n(z,t) \tag{1.19}$$

Assuming initial condition $n(z,0) = n_0(z)$, the solution of (1.19) is

$$n(z,t) = exp\left(\frac{t\mu\rho}{\epsilon}\right) n_0 \left(exp\left(\frac{t\mu\rho}{\epsilon}\right) z - \frac{L}{2}\left[exp\left(\frac{t\mu\rho}{\epsilon}\right) - 1\right]\left(1 - \frac{\rho_m}{\rho}\right)\right) \tag{1.20}$$

As can be seen from the solution (1.20) the electron distribution changes its shape in time. The first exponential (in product with initial condition n_0) changes the "height" of the distribution, while the second exponential (multiplying z) causes the broadening or shortening of the initial distribution. This may not be apparent, but if we choose the initial distribution to be Gaussian, the second exponential can be joined with variance σ as can be seen below.

$$n_0(z) = \frac{1}{S\sqrt{\pi}\sigma} exp\left(-\frac{x^2}{\sigma^2}\right) \tag{1.21}$$

$$n(z,t) = \frac{1}{S\sqrt{\pi}\sigma} exp\left(\frac{t\mu\rho}{\epsilon}\right) exp\left(-\frac{(z-\gamma)^2}{\left(\sigma\, exp\left(-\frac{t\mu\rho}{\epsilon}\right)\right)^2}\right) \tag{1.22}$$

$$\gamma = \frac{L}{2}\left(1 - exp\left(-\frac{t\mu\rho}{\epsilon}\right)\right)\left(1 - \frac{\rho_m}{\rho}\right)$$

Now we can see that the variance $\sigma' = \sigma\, exp\left(-\frac{t\mu\rho}{\epsilon}\right)$, changes with time and therefore, the distribution of electrons is broadening ($\rho < 0$), shortening ($\rho > 0$) or stays the same ($\rho = 0$). Change of the electron distribution shape is shown in Fig. 1.4. The $t_{r\,1/2}$ in Fig. 1.4 represents the time the charge carriers require to get to the half of the sample.

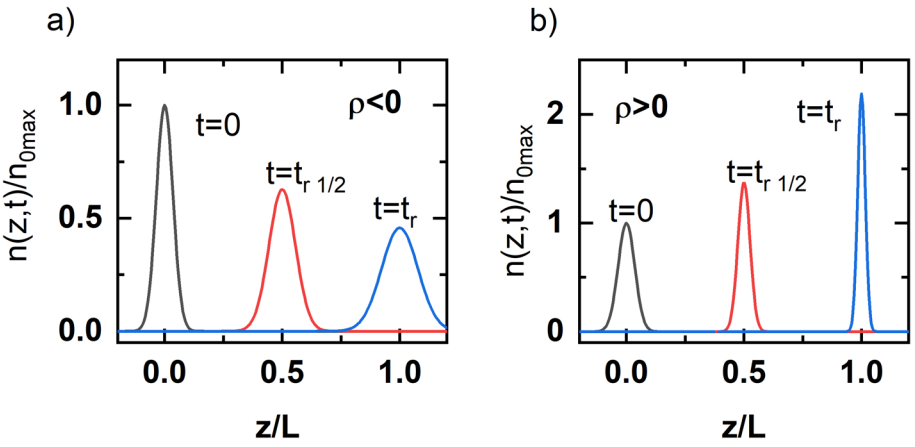

Fig. 1.4: a) Broadening ($\rho < 0$) and b) shortening ($\rho > 0$) of the carrier distribution due to the non-constant electric field. Distributions are normalized with respect to the maximum of initial distribution $n(0,0) = n_{0max}$.

In order to obtain the shape of the current waveform, a sharply localized electron cloud is assumed and equation (1.10) is used. The final current waveform is then

$$I(t) = Q_0\mu_e E_0\left(1 - \frac{\rho}{\rho_m}\right) exp\left(-\frac{\mu_e\rho}{\epsilon}t\right)\chi(t,0,t_r), \tag{1.23}$$

where transit time t_r is given by

$$t_r = \frac{t_{r0}}{2}\frac{\rho_m}{\rho} ln\left(\frac{\rho_m + \rho}{\rho_m - \rho}\right), \tag{1.24}$$

If the charge density is equal to $\pm\rho_m$ then transit time goes to infinity. In both cases, electrons cannot reach the anode either because they recombine at the anode ($\rho \geq \rho_m$) and no signal is detected or they are stopped in the inactive layer ($\rho \leq -\rho_m$). Infinite transit time represents itself as the vanishing of the sharp decrease of the

waveform as can be seen in Fig. 1.5. Another effect of space charge is the prolongation of the transit time – transit time is the shortest in the presence of no space charge and with the increase of charge density ρ transit time prolongs regardless the sign of the space charge ρ.

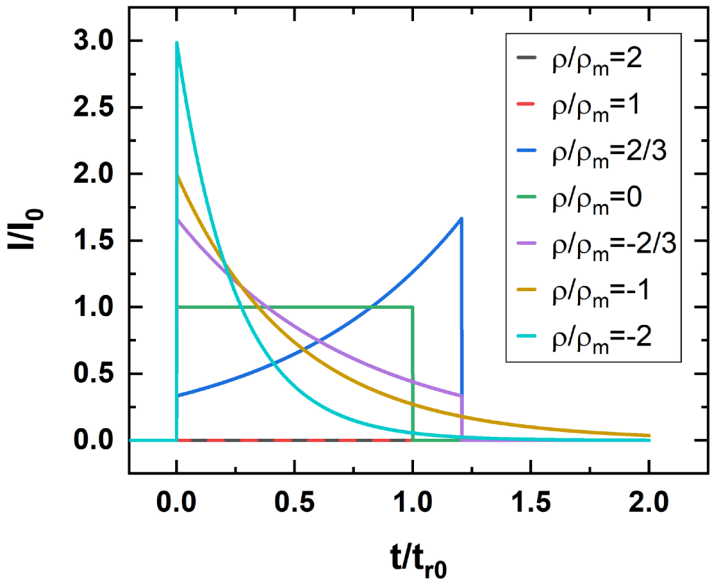

Fig. 1.5: Normalized current waveforms calculated for different space charge distributions $\rho(z)$.

1.3 Effects of charge trapping and detrapping

The charge collection is significantly influenced by the presence of crystal defects e.g. impurities or point defects. These defects are often described by the Shockley-Read-Hall model [10], which is schematically shown in Fig. 1.6. Disregarding the band-to-band recombination and photo-excitation there are four processes that can occur – a) capture of the free electron from conduction band by a defect, b) thermal emission of electron back to the conduction band, c) capture of the free hole from the valence band by a defect and d) thermal emission a hole back to the valence band. Rates of processes a)-d) are given by formulas [9],[11]

$$p_a = v_{th}^n \sigma_n (N_{t0} - N_t) n = \frac{n}{\tau_t^n}, \tag{1.25}$$

$$p_b = v_{th}^n \sigma_n N_C \, exp\left(-\frac{E_t}{k_B T}\right) N_t = \frac{N_t}{\tau_d^e}, \tag{1.26}$$

$$p_c = v_{th}^p \sigma_p N_t p = \frac{p}{\tau_t^h}, \tag{1.27}$$

$$p_d = v_{th}^p \sigma_p N_V exp\left(-\frac{E_g - E_t}{k_B T}\right) (N_{t0} - N_t) = \frac{N_{t0} - N_t}{\tau_d^h}, \tag{1.28}$$

where v_{th}^{n}, σ_n (v_{th}^{p}, σ_p) are thermal velocity and capture cross-section of electrons (holes), N_{t0} is the concentration of all states of level E_t, N_t is the concentration of all occupied states of level E_t, N_C (N_v) is the effective density of states in the conduction (valence) band, k_B is Boltzmann constant, T is the absolute temperature of the crystal and E_g is the bandgap of the semiconductor.

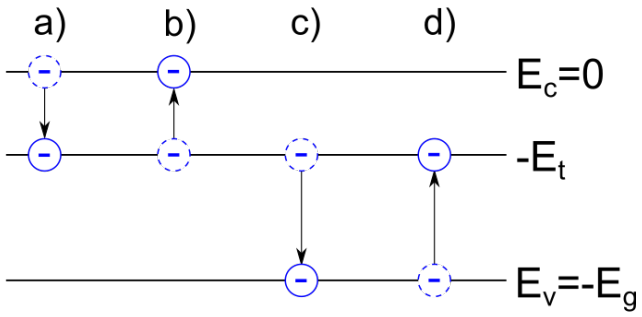

Fig. 1.6: Band diagram of the possible defect described by the Shockley-Read-Hall model, where E_t is the energy of trapping center and E_c (E_v) represents conduction (valence) band and E_g is the width of the bandgap of the semiconductor.

If the rate of thermal emission of an electron from level E_t back to the conduction band (1.26) is much higher than the rate of recombining with a hole (the rate of hole capture by the defect E_t) (1.27) then the defect E_t is usually identified as the trapping centre and processes a) and b) as electron trapping and detrapping, respectively. Similarly, hole trapping and detrapping are introduced. On the other hand, if the rate (1.26) is smaller than the rate (1.28) the level E_t is considered to be recombination centre. Another classification of trapping centers depends on the rate of detrapping – if the detrapping time is significantly faster than transit time the trapping centre is called shallow (due to its distance from conduction or valence band) or deep trapping centre in the opposite case.

Let's begin with one shallow trap described by trapping time τ_t (1.25) and detrapping time τ_d (1.26) and also assume that both trapping and detrapping times are spatially independent and that their temporal change during the flight of probing carriers is negligible. The evolution of the trapped n_1 and "free" electrons in the conduction band n_0 in constant electric field can then be described by differential equations

$$\frac{\partial n_0(z,t)}{\partial t} = -v_0 \frac{\partial n_0(z,t)}{\partial z} - \frac{n_0(z,t)}{\tau_t} + \frac{n_1(z,t)}{\tau_d} \tag{1.29}$$

$$\frac{\partial n_1(z,t)}{\partial t} = \frac{n_0(z,t)}{\tau_t} - \frac{n_1(z,t)}{\tau_d} \tag{1.30}$$

Both equations were obtained from equation (1.7) by disregarding diffusion and assuming that trapped electrons cannot move. Nevertheless, finding the solution to this system is difficult, so some discussion is needed. In order to simplify the equation (1.29) spatial dependence (the first term in equation (1.29)) is neglected. However, the solution will be valid only for the time smaller than t_{r0} (for sharply localized electron distribution), because until t_{r0} all the charge carriers are moving with constant drift velocity v_0 and after the t_{r0} the never-trapped charge carries exit the detector. The dynamics until this point can be imagined as the two-level system that is slowly reaching its equilibrium distribution of carries. With this in mind, the equations (1.29) and (1.30) transform to

$$\frac{\partial n_0(t)}{\partial t} = -\frac{n_0(t)}{\tau_t} + \frac{n_1(t)}{\tau_d}, \tag{1.31}$$

$$\frac{\partial n_1(t)}{\partial t} = \frac{n_0(t)}{\tau_t} - \frac{n_1(t)}{\tau_d}, \tag{1.32}$$

with initial condition $n_0(0) = N_0$ and $n_1(0) = 0$. The solution of this system is then

$$n_0(t) = \frac{N_0}{(\tau_t + \tau_d)}\left[\tau_t + \tau_d \, exp\left(-t\left(\frac{1}{\tau_t} + \frac{1}{\tau_d}\right)\right)\right] \quad t < t_{r0} \tag{1.33}$$

$$n_1(t) = \frac{N_0 \tau_d}{(\tau_t + \tau_d)}\left[exp\left(-t\left(\frac{1}{\tau_t} + \frac{1}{\tau_d}\right)\right) - 1\right] \quad t < t_{r0} \tag{1.34}$$

After the application of the Shockley-Ramo theorem (1.10) the shape of the current waveform is obtained

$$I(t) = \frac{Q_0 v_0}{(\tau_t + \tau_d)L}\left[\tau_t + \tau_d \, exp\left(-t\left(\frac{1}{\tau_t} + \frac{1}{\tau_d}\right)\right)\right] \; t < t_{r0} \tag{1.35}$$

For the case of deep trap ($\tau_d \to \infty$) this waveform can be simplified to purely exponential form and since no detrapping is taking place, the waveform for $t > t_{r0}$ is equal to zero

$$I(t) = \frac{Q_0 v_0}{L} exp\left(-\frac{t}{\tau_t}\right) \chi(t, 0, t_{r0}). \tag{1.36}$$

Current waveforms for different trapping and detrapping times are shown in Fig. 1.7.

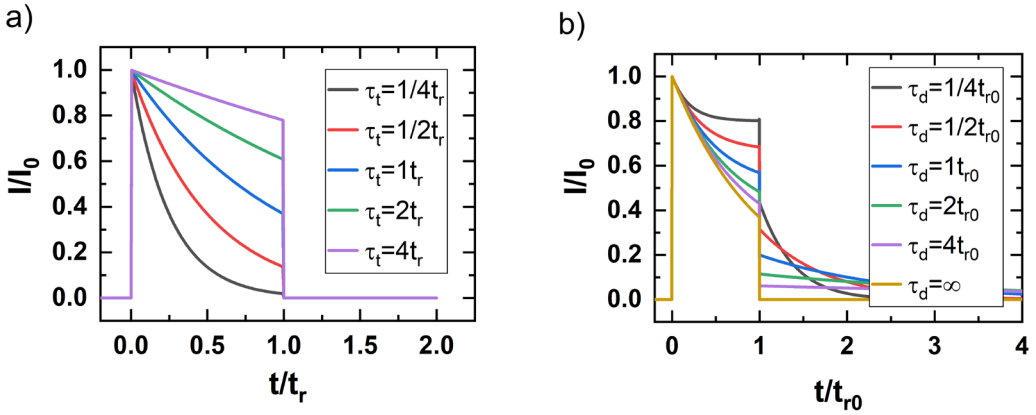

Fig. 1.7: Normalized current waveforms a) for different trapping times τ_t and no detrapping (deep trap) and b) for $\tau_t = t_r$ and different de-trapping times τ_d (shallow trap).

1.3.1Approximation beyond transit time

The carrier trapping and subsequent detrapping changes the initial distribution of charge carriers. Due to this current tail induced by detrapped carriers should be observed beyond the transit time. As was discussed earlier the analytical solution of system (1.29), (1.30) beyond transit time does not exist so approximative solution must be found.

Let's start again with equations (1.37), but this time we dismiss detrapping and try to calculate the distribution of trapped carriers $n_1^1(z,t)$. The detrapping term in equation (1.29) is basically an interaction term and ties both equations together, by eliminating it is possible to solve both gradually.

$$\frac{\partial n_0^0(z,t)}{\partial t} = -v_0 \frac{\partial n_0^0(z,t)}{\partial z} - \frac{n_0^0(z,t)}{\tau_t}$$
$$\frac{\partial n_1^1(z,t)}{\partial t} = \frac{n_0^0(z,t)}{\tau_t} - \frac{n_1^1(z,t)}{\tau_d} \qquad (1.37)$$

Solutions of the system (1.37) are given by

$$n_0^0(z,t) = \frac{N_0}{S} exp\left(-\frac{t}{\tau_t}\right)\delta(z - tv_0)\chi(z,0,L)\theta(t) \qquad (1.38)$$

$$n_1^1(z,t) = \frac{N_0}{Sv_0\tau_t} exp\left(-\frac{z}{\tau_t v_0}\right) exp\left(-\frac{t-\frac{z}{v_0}}{\tau_d}\right)\times$$
$$\times\, \chi(z,0,L)\theta(tv_0 - z), \qquad (1.39)$$

where $\theta(\mathrm{tv}_0 - \mathrm{z})$ is Heaviside theta. In the k-th iteration the distribution of the $(k-1)$-times trapped carriers is used as detrapping or generation term, as can be seen in the system below.

$$\begin{aligned} \frac{\partial n_0^k(z,t)}{\partial t} &= -v_0 \frac{\partial n_0^k(z,t)}{\partial z} - \frac{n_0^k(z,t)}{\tau_t} + \frac{n_1^{k-1}(z,t)}{\tau_d} \\ \frac{\partial n_1^{k+1}(z,t)}{\partial t} &= \frac{n_0^k(z,t)}{\tau_t} - \frac{n_1^{k+1}(z,t)}{\tau_d} \end{aligned} \tag{1.40}$$

The first iteration solution of once detrapped carries $\mathrm{n}_0^1(\mathrm{z},\mathrm{t})$ using the equation (1.39) and the system (1.40) is given by

$$n_0^1(z,t) = \frac{z}{v_0 \tau_d} n_1^1(z,t) \tag{1.41}$$

The process of evaluation of the current waveform is the same as before except this time it is necessary to add all the contributions up (never trapped carriers, once detrapped, …)

$$I^0(t) = \frac{Q_0 v_0}{L} exp\left(-\frac{t}{\tau_t}\right) \chi(t,0,t_r) \tag{1.42}$$

$$\begin{aligned} I^1(t) = \frac{Q_0 v_0}{L} \frac{\tau_d \tau_t}{(\tau_t - \tau_d)^2} exp\left(-\frac{t}{\tau_d}\right) \Big[& \beta(t) \chi(t,0,t_r) \\ & + \beta\left(\frac{L}{v_0}\right) \theta(t - t_r) \Big] \end{aligned} \tag{1.43}$$

$$\beta(\mathrm{t}) = 1 - \left[1 + t\left(\frac{1}{\tau_\mathrm{t}} - \frac{1}{\tau_d}\right)\right] exp\left[-t\left(\frac{1}{\tau_\mathrm{t}} - \frac{1}{\tau_d}\right)\right]$$

As can be seen from (1.43) the tail in the first approximation is exponentially damped as $exp\left(-\frac{t}{\tau_d}\right)$. The first approximation is valid only if the charge carrier is on average trapped half-times since we are only counting never trapped and once trapped carriers. With the same logic, the k-th order approximation is valid if carriers are on average trapped $\frac{k}{2}$-times $\left(\frac{0+1+2+\cdots+k}{k+1} = \frac{k}{2}\right)$. Trapping time can be also defined as an average time carrier is drifting before it is trapped and de-trapping time as an average time carrier spends in the trap. Now we can calculate how many times on average carrier is trapped during flight through the detector $N(t)$ (until the time t)

$$N(t) = \frac{t}{\tau_t + \tau_d} \tag{1.44}$$

Knowing this, the k-th order approximation is valid until the time $t_{lim} = \frac{k}{2}(\tau_t + \tau_d)$. Beyond this time higher-order approximations have to be used.

Given the used approach the approximated current waveform will always be lower than the precise solution, as it can be clearly seen in Fig. 1.8. However, for the case of the constant electric field, distributions of k-times detrapped carriers n_0^k can be summed up and precise solution of the system (1.29) and (1.30) with initial condition $n(z,0) = \frac{N_0}{S}\delta(z)$ can be obtained. The result of the summation (computed in Wolfram Mathematica) is given by

$$n_0(z,t) = n_0^0(z,t) + n_0{}'(z,t)$$

$$n_0{}'(z,t) = \sum_{k=1}^{\infty} n_0^k(z,t)$$

$$n_0{}'(z,t) = \frac{N_0}{S}\frac{\sqrt{z}}{v_0\sqrt{\tau_t\tau_d(tv_0 - z)}}exp\left(-\frac{t}{\tau_d} - \frac{z}{v_0}\left(\frac{1}{\tau_t} - \frac{1}{\tau_d}\right)\right) \times J_1\left(2\frac{\sqrt{(tv_0 - z)z}}{v_0\sqrt{\tau_t\tau_d}}\right)\theta(tv_0 - z)\chi(z,0,L) \quad (1.45)$$

where J_1 is the modified Bessel function of the first kind of order one. A similar result obtained by a different method (probability calculations) was obtained by Tefft [12]. The same approach as above can be used for multiple trapping centres and even for the non-constant electric field.

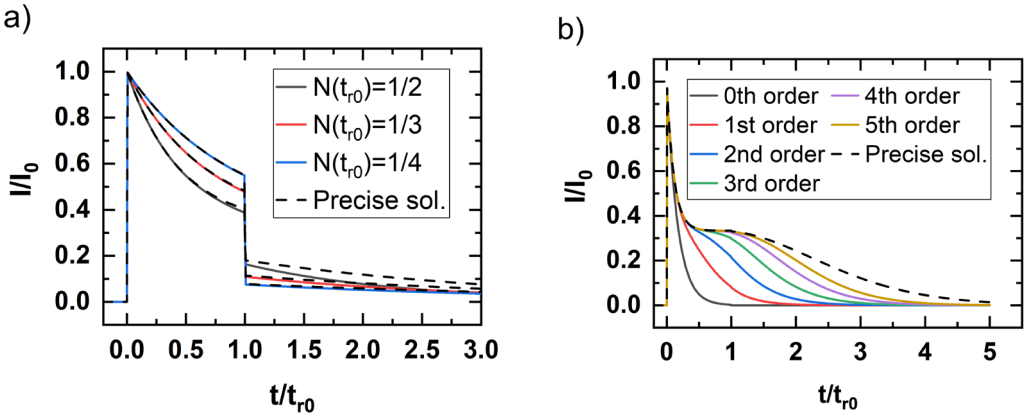

Fig. 1.8: a) Comparison of the first-order approximation with the precise analytical solution (dashed) (1.45) for different average trapping $\left(\tau_t = \frac{1}{2}\tau_d\right)$ and b) convergence of the higher-order approximations $\left(\tau_t = \frac{1}{2}\tau_d = \frac{1}{6}t_{r0}\right)$.

1.3.2Trap controlled mobility

As can be seen in Fig. 1.8 b) the presence of a shallow trap can impede the mobility evaluation since carriers reach the opposite electrode much later than the default transit time t_{r0}. In this case, the effective mobility that accounts for trapping and detrapping phenomena that slow down the carriers is introduced [12], [13]. The lower limit of the effective mobility can be calculated as the fraction of the time carrier spends drifting during one trapping cycle ($\tau_t + \tau_d$)

$$\mu_{eff} = \mu_0 \frac{\tau_t}{\tau_t + \tau_d} \tag{1.46}$$

The formula (1.46) is valid only in the case when the density of the free carriers is in equilibrium with the respective trap. This condition represents the situation when the number of trapping events $N(t_r) \gg 1$. As can clearly be seen in Fig. 1.9a) the effective mobility is double the drift mobility when trapping and detrapping times are equal, but only after the steady concentration of free carriers was reached (the flat part of the waveforms). In Fig. 1.9b) waveforms for different detrapping times are shown clearly demonstrating formula (1.46).

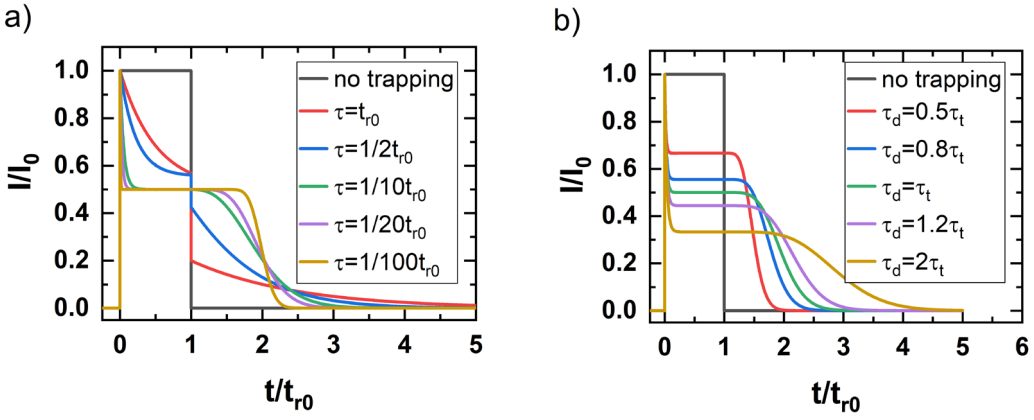

Fig. 1.9: a) Normalized current waveform with different (de-) trapping ($\tau = \tau_t = \tau_d$) and b) increase of the transit time t_r due to the effective mobility $\left(\tau_t = \frac{1}{20} t_{r0}\right)$.

1.4 Surface recombination

The photogenerated charge can recombine in the surface layer due to the presence of surface states. The rate of this recombination is often different than the rate of the recombination in the bulk material. The effect of the surface can be described by the velocity of the surface recombination s. Let's assume that all carriers are photogenerated in the thin surface layer and let p_b be the probability of their transition into the bulk material. Levi et al. [14] assumed that the ratio of the "bulk" carriers to

recombined carriers is equal to the ratio of drift velocity v and the velocity of the surface recombination [15]

$$\frac{p_b}{1-p_b} = \frac{v}{s}. \tag{1.47}$$

The probability of the carrier entering bulk is then

$$p_b = \frac{1}{1+\frac{s}{v}} \tag{1.48}$$

Since the carrier recombination is taking place in the very thin region, its effect on the shape of the current waveform can be neglected and only the decrease of the collected charge Q_0 (assuming no trapping) described by the equation (1.49) is observed.

$$Q_0(E) = \frac{Q_{00}}{1+\frac{s}{\mu\, E(0)}} \tag{1.49}$$

The Q_{00} is the photogenerated charge and drift velocity $v = \mu\, E(0)$ was substituted (assuming that the charge is generated at $z = 0$). Because of this, surface recombination cannot be recognized from one waveform but bias dependence has to be measured.

The bias-normalized current waveforms for a constant electric field are shown in Fig. 1.10. Bias-normalization was done to visualize the effect of surface recombination, since the current is normally linear in bias, as can be seen in equations (1.15) and (1.16).

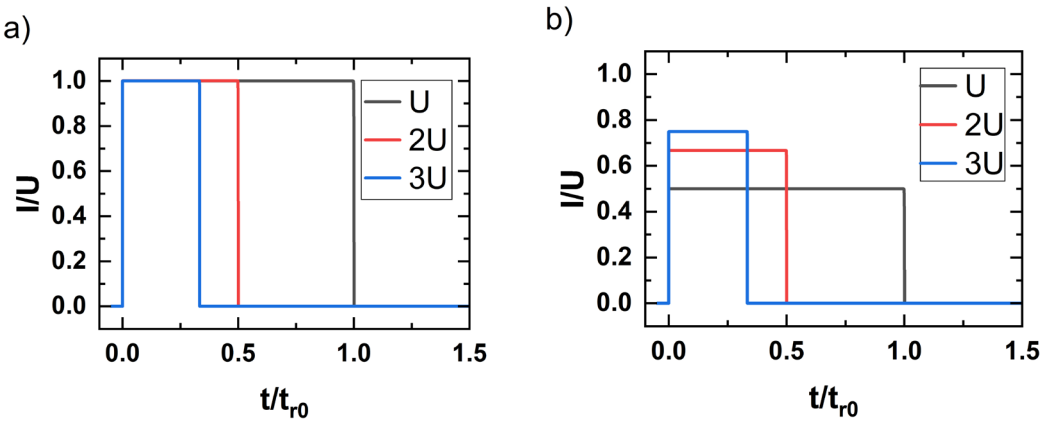

Fig. 1.10: Current waveforms normalized by bias for the model a) without surface recombination and b) with surface recombination

1.5 Charge collection efficiency

Charge collection efficiency (CCE) is one of the most important parameters for evaluation of the detector quality, defined as a fraction of collected charge to the generated charge. For deep-level trapping od the carriers the CCE can be described by the single carrier Hecht equation (assuming strong absorption and constant electric field) [16]

$$CCE = \frac{\tau}{t_r}\left[1 - exp\left(-\frac{t_r}{\tau}\right)\right], \tag{1.50}$$

where τ is the carrier lifetime, or by modified Hecht equation that involves surface recombination [15]

$$CCE = \frac{\tau}{t_r}\frac{1}{1+\frac{s}{v}}\left[1 - exp\left(-\frac{t_r}{\tau}\right)\right]. \tag{1.51}$$

2 Laser-induced Transient Current Technique

The laser-induced transient current technique (L-TCT) belongs to the family of the Time-of-Flight measurements and is commonly used to evaluate detector properties e.g. carrier mobility, lifetime, electric field profile in the detector, etc. [17]–[19]. This method is based on measuring the current response generated by short laser pulses. Laser pulses create electron-hole pairs, that drifts in an applied electric field to corresponding electrodes. Due to Shockley-Ramo theorem [8], photogenerated carriers induce electric current on the electrodes, which is subsequently measured by an oscilloscope. Using this technique, it is possible to trigger oscilloscope directly to the laser pulse itself rather than the rising edge of the current pulse as it is in the case of untriggered sources (alfa, gamma). This allows for faster and easier data acquisition and as a result higher signal-to-noise ratio. Our experimental setup is shown in Fig. 2.1. Above-bandgap laser pulses (2ns FWHM) are provided by SuperK Compact Supercontinuum white laser combined with 670nm bandpass filter. The optical part of the setup is completed with a neutral density filter, which attenuates laser intensity. High laser intensity leads to more effects, one of which is a plasma effect that significantly complicates the data processing.

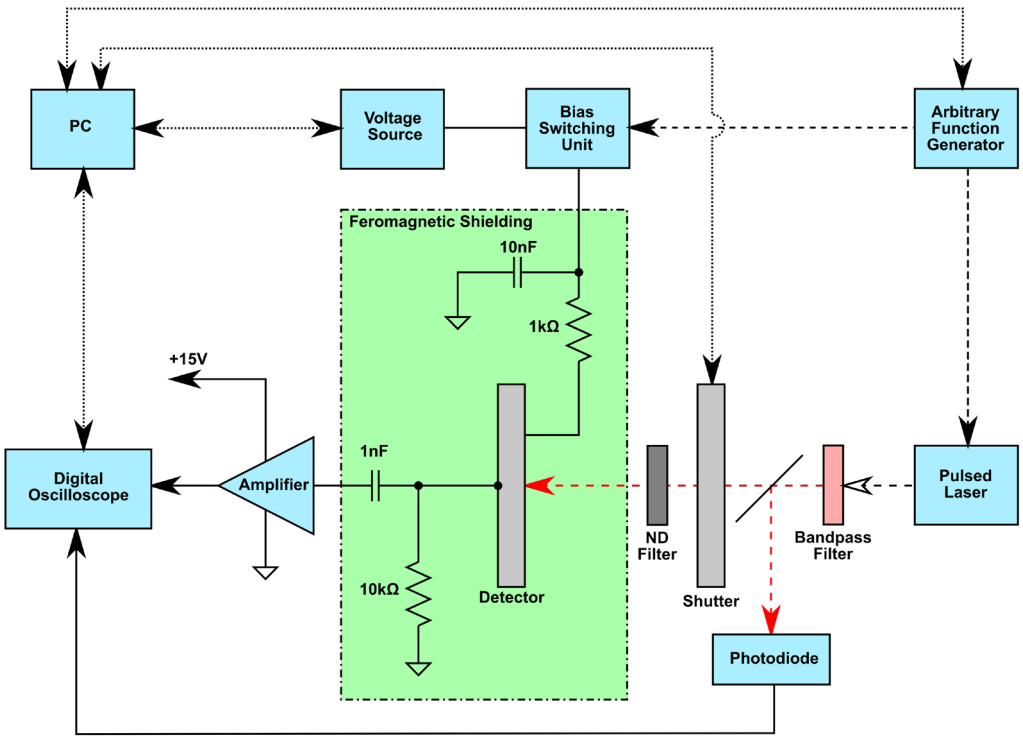

Fig. 2.1: Scheme of our L-TCT setup

We are also using masks, placed in front of the detector, to avoid illuminating edges of the detector. Masks presented in Fig. 2.2, are also used to avoid unintentional illumination of the area near the guard ring. Guard ring is surrounded by the non-conducting region that separates the guard ring electrode and central pixel which effectively minimizes the effect of surface leakage current. The laser is focused at the centre of the detector forming a 1mm^2 spot. For the continuous above-bandgap LED (660nm) illumination a square mask with roughly 25mm^2 was used.

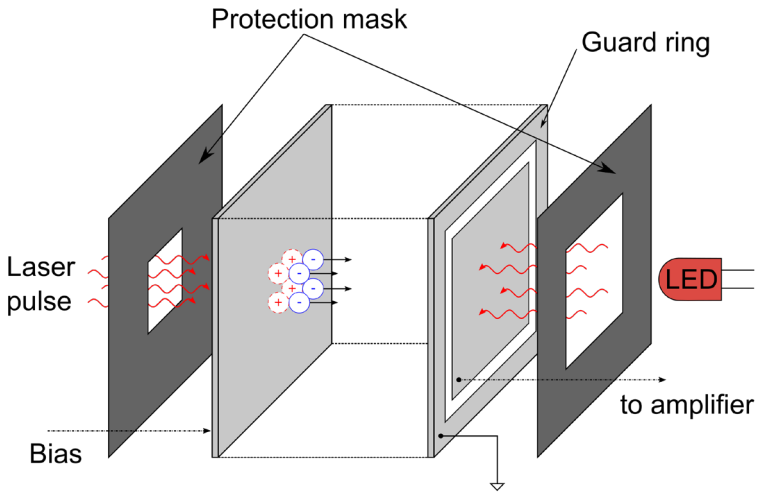

Fig. 2.2: Masking of the detector

As a source of a high voltage source, the Sorensen XG 6001.4 is used combined with custom-made bias switching unit capable operating at maximal frequency 500Hz and maximal bias of $\pm$1500V. Both the switching unit and the continuum laser are controlled by arbitrary function generator Tektronix AFG 3252. By applying pulsed bias with a sharp rising edge (80µs) and sufficient depolarization time, it is possible to suppress the effect of dark current polarization and by varying the relative position of the laser pulse and the rising edge it is possible to observe space charge formation with great time resolution. Schematics of the relative position of the laser and the bias pulse are shown in Fig. 2.3. In addition, the shutter is used to temporarily block the laser beam for the measurement of the background (dark) current. Background can be then conveniently subtracted from the waveform which eliminates triggered noise and distortion by the dark current. Oscilloscope (LeCroy WaveRunner 640Zi), arbitrary function generator, shutter and voltage source are all controlled by computer, allowing full automation of the measurement.

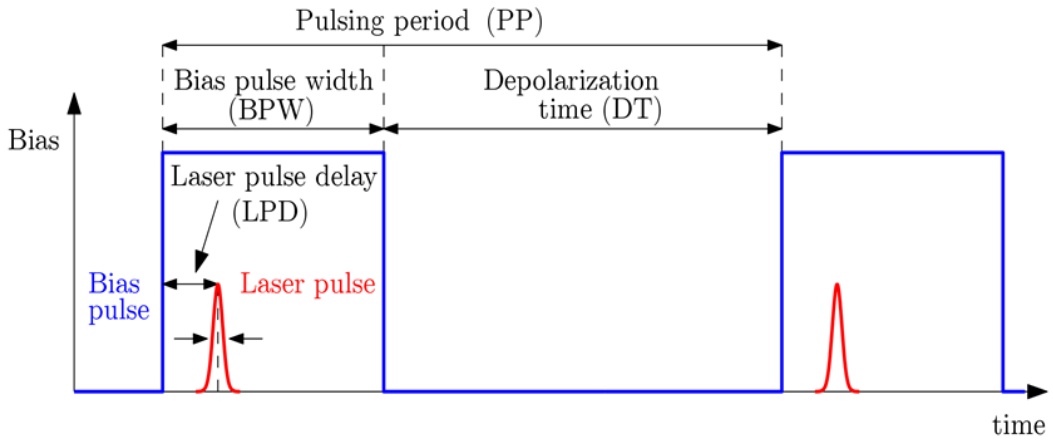

Fig. 2.3: Relative position of bias and laser pulse [20]

Due to low laser intensities, the current response needs to be amplified and only then it can be recorded by an oscilloscope. However, the use of the amplifier brings out another problem – the measured data are distorted by the transfer function of the electronic circuit. To obtain the original signal, the deconvolution method from [21] is used.

Due to using a detector with a guard-ring contact structure in the anode, there are four different configurations for L-TCT measurement shown in Fig. 2.4. To simplify the following text we use abbreviations FSe for measurement of electron signal, while the full/front side (FS) of the detector is illuminated; GRSh for measurement of hole signal while guard-ring side (GRS) of the detector is illuminated. The evolution of the space charge in both of these case is the same since the electric field has the same direction. Similarly, FSh is the measurement of the hole signal while the FS is illuminated and GRSe is the measurement of the electron signal while the GRS is illuminated. L-TCT measured in both polarities can give insight into the properties of the contacts.

For the transition from FSe to GRSh geometry, it is required to turn the detector around and switch the bias polarity, due to the design of our electronics setup. If the detector is also simultaneously LED illuminated, during the FSe to GRSh transition the LED have to be also removed and plugged back in at the opposite side in order not to change which electrode is LED illuminated.

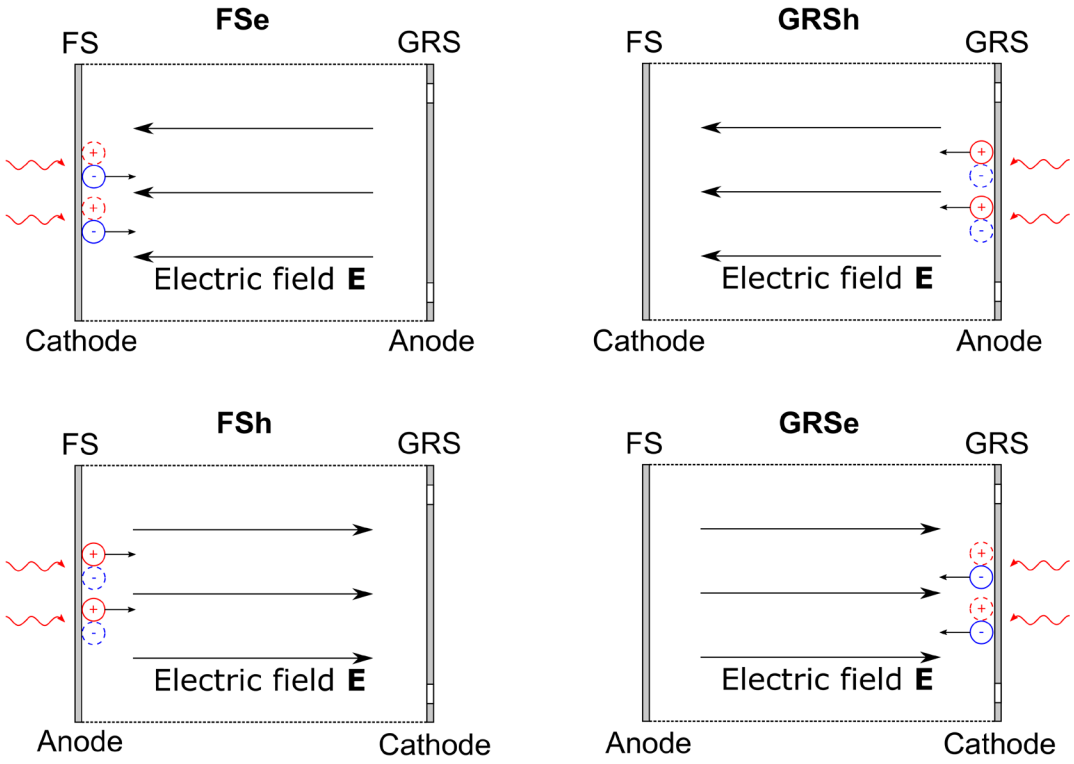

Fig. 2.4: Experimental setup configuration of the measurement of the electron (FSe, GRSe) and hole (GRSh, FSh) signals.

2.1 Monte Carlo simulation

In many cases solving the transport equation (1.7) is difficult, if one would assume a system with two trapping centres, the solution would become extremely complex and beyond the transit time, the analytical solution would not exist at all. Therefore, for the evaluation of transport properties, Monte Carlo (MC) simulation is used [18],[22] or drift-diffusion and Poisson equation have to be solved numerically [9]. We are using one dimensional MC simulation based on [18] with the addition of arbitrary electric field, diffusion and variable laser pulse parameters (width, absorption).

For the MC simulation, we use the following assumptions. Firstly, the N charge carriers are randomly generated with their initial position satisfying the Lambert-Beer law. Probability of the carrier being generated at initial position z is [20]

$$p_z(z) = \frac{\alpha}{1 - exp(-\alpha L)} exp(-\alpha z)\chi(z, 0, L), \qquad (2.1)$$

where the fraction is just the normalization term and $\chi(z, 0, L)$ ensures that the carriers are generated only inside the detector. Similarly, the probability of carrier generation by a square laser pulse with the width of t_{laser} at the time t is given by (2.2). However, it is possible to use any arbitrary temporal distribution $\mathrm{p_t}$.

$$p_t(t) = \frac{1}{t_{laser}} \chi(t, 0, t_{laser}). \tag{2.2}$$

The photogenerated charge Q_0 is divided among N carriers. The surface recombination is included by introducing the bias (electric field E) dependence of $Q_0(E)$ described by equation (1.49).

Each time step δt of the simulation, only the free carriers drifts the distance δz

$$\delta z = \mu E(z)\delta t + u\,, \tag{2.3}$$

where $E(z)$ is the arbitrary electric field and u is the contribution of the carrier diffusion described by the diffusion coefficient D and probability distribution [20]

$$p_u = \frac{1}{\sqrt{4\pi D\delta t}}\, exp\left(-\frac{u^2}{4D\delta t}\right). \tag{2.4}$$

The MC current waveforms consist of the contributions of all the carriers, on which the Shockley-Ramo theorem was applied.

Carrier traps are described by their respective trapping $\tau_{trapping}$ and detrapping time $\tau_{detrapping}$, that defines the probability of carrier (de)trapping in time step δt

$$p_{(de)trapping} = \frac{\delta t}{\tau_{(de)trapping}}. \tag{2.5}$$

Usually, two trap model (one deep and one shallow trap) is used to describe the trapping and detrapping phenomena. A detailed description of our MC simulation can be found in [20].

3 Results and discussion

3.1 Detector preparation

The detectors for this thesis were provided by Redlen Technologies. The detectors were prepared by from semi-insulating indium-doped CdZnTe single crystal with 10% of Zn, which was grown by Traveling Heater Method. Scheme of the used detector with its physical dimensions is shown in

Fig. 3.1. The planar detector has platinum electrical contacts with a guard ring structure on one side. The uncontacted surface was coated by an epoxy passivation layer.

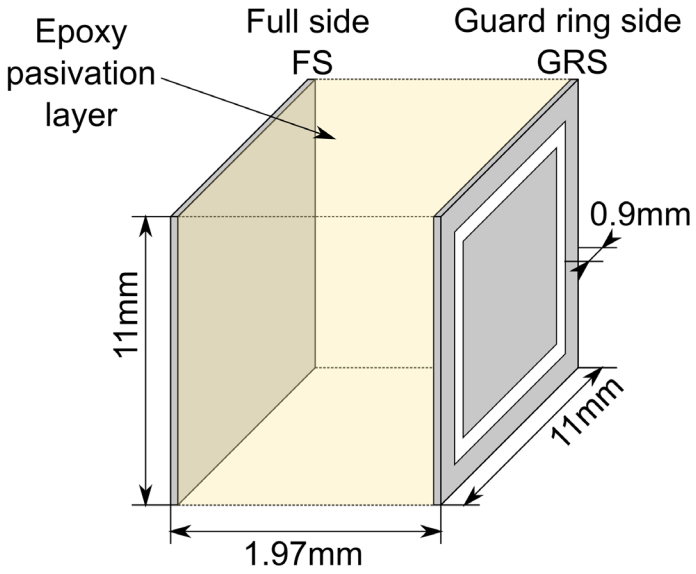

Fig. 3.1: Physical dimensions of the detector

3.2 I-V characteristics measurement

The I-V characteristic measurement of Redlen detector curve presented in Fig. 3.2 shows clear rectifying Schottky behaviour with reverse direction for negative bias applied to the full electrode side (FS). This result was surprising for us because both electrodes are prepared by the same method using platinum, as was declared by the vendor. Probably a different (for us) unknown surface treatment was applied for each side of the detector by Redlen.

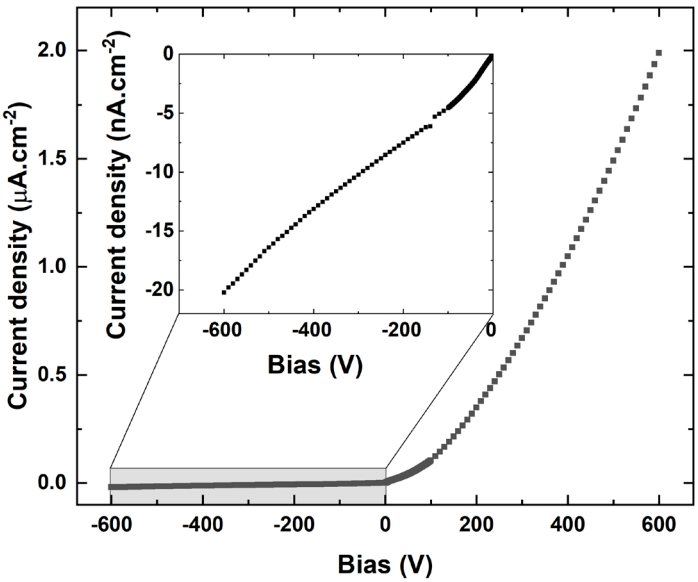

Fig. 3.2: Current-voltage characteristic. Bias was applied to the full electrode side (FS). Inset shows detail of the I-V characteristics with negative polarity

3.3 L-TCT measurement in the dark

Current waveforms in this thesis were measured only in the FSe or GRSh geometry (see Fig. 2.4). In both of these, the electric current flows in the negative direction of *z* axis resulting in negative current in the waveforms. In order to adhere to the "upward waveform" convention and keep the correct sign of the current, the waveforms are shown negative side up.

L-TCT was used in the dark (no continuous illumination) and under continuous LED illumination. Before the L-TCT measurement was done, we had to find the correct conditions for the measurement of the current waveforms. Firstly, if we want to measure the unpolarized detector, the laser time delay – LPD (see Fig. 2.3) has to be short enough to acquire the data before the space charge is formed. We found that for the LPD in the interval 80μs-150μs the current waveforms are the same, it means that no significant space charge affecting the shape of the waveforms was formed. For the measurement in the unpolarized detector, the LPD=80μs was chosen.

The second parameter is the depolarization time (DT), which is the bias-off time in Fig. 2.3. The DT has to be long enough, for the complete depolarization of the detector. The DT is most reliably measured in the polarized detector when the current

waveform is curved and the transit time is sensitive to small variations of charge density. In the measurement itself 1s wide bias pulse (BPW) and 900ms laser pulse delay (LPD) was used while a set of waveforms for different DT was measured. Suitable DTs are the ones, for which the current waveforms are the same. For short DT the detector does not depolarize completely, therefore the next measured waveform is affected by the space charge formed during the previous bias pulse. This way the depolarization time of 100ms was found, but for long-lasting measurements, 500ms was used to eliminate a chance of a slow space charge build-up.

The third parameter - appropriate laser pulse intensity, was found similarly. A set of current waveforms was measured for different intensities starting with lowest to highest. After their comparison, we found the most suitable intensity for L-TCT measurement. For lower intensities, the current waveforms were lost in the noise and for higher intensities, they were significantly affected by the plasma effect [23].

3.3.1 Measurement in the unpolarized detector

The unpolarized current waveforms measured in the FSe geometry are presented in Fig. 3.3. Black dashed lines represent the MC fit. The electric field profile obtained by the MC simulation is shown in the inset of Fig 3.3. It was found, that electron waveforms are completely flat in each used bias which points to the fact that the detector is indeed unpolarized (see subsection 1.2.1). Therefore, an assumption that for the $\mathrm{LPD} = 80\mu\mathrm{s}$ detector is not polarized is correct. The measured electron waveforms were flat even for -20V so only the lower limit of the electron lifetime was estimated as $\tau_e \gg 2\mu\mathrm{s}$ (transit time of the -20V waveform).

The hole waveforms measured in the unpolarized detector in GRSh geometry are shown in Fig. 3.4. The electric field profile obtained by the MC simulation is shown in the inset in Fig. 3.4 and the fits themselves are displayed as black dashed lines. As was discussed earlier the electric field in the GRSh geometry is the same as in the FSe, therefore, the hole waveforms were also measured in the unpolarized detector. Because of this, the curvature of the hole waveforms can be entirely ascribed to carrier trapping. Since the hole tails are observed, the two-level model with one deep and one shallow trap was used for MC fitting. The transport parameters obtained by the MC simulation are shown in Table 3.1.

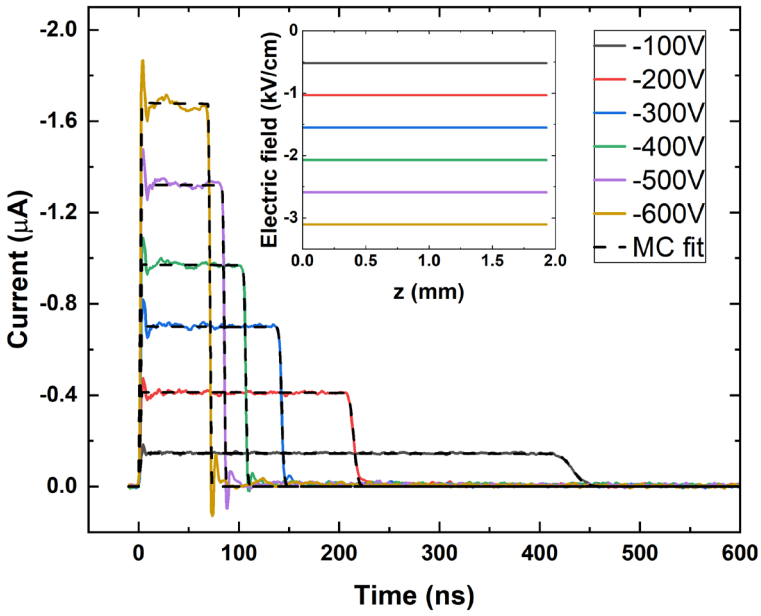

Fig. 3.3: Pulsed bias dependence of electron current waveforms in FSe geometry using LPD = $80\mu s$. Black dashed lines represent the fit by MC simulation. Electric field profile obtained by MC simulation is shown in the inset.

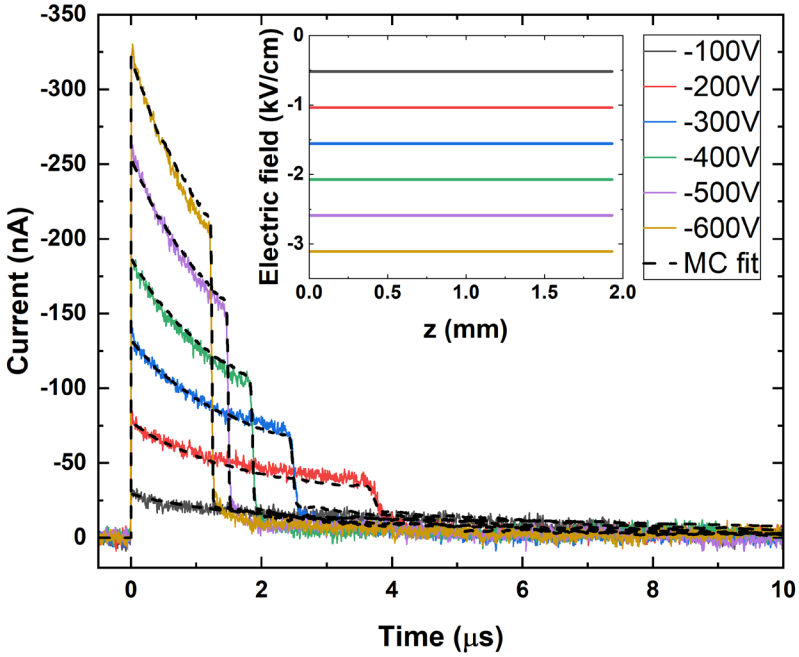

Fig. 3.4: Pulsed bias dependence of the hole current waveforms in GRSh geometry using LPD = $80\mu s$. Black dashed lines represent the fit by MC simulation. Electric field profile obtained by MC simulation is shown in the inset.

Table 3.1: Transport properties of the unpolarized detector obtained by MC simulation

	Electrons	Holes
Carrier mobility μ ($\mathrm{cm^2.V^{-1}.s^{-1}}$)	950	50
Deep level trapping time $\tau_{t\ deep}$ (μs)	$\gg 2$	20
Deep level detrapping time $\tau_{d\ deep}$ (μs)	could not be evaluated	$\gg 10$
Shallow level trapping time $\tau_{t\ shallow}$ (μs)	$\gg 2$	2.7
Shallow level detrapping time $\tau_{\ d\ shallow}$ (μs)	could not be evaluated	3

The bias-normalization of the electron Fig. 3.3 and hole Fig. 3.4 current waveforms are shown in Fig. 3.5. The individual normalized waveforms have each different height because some part of the photogenerated carriers recombined in the surface layer. To evaluate the velocity of the surface recombination of electrons s_e, the measured current waveforms were firstly integrated to obtain the collected charge. Bias dependence of the collected charge was then fitted by the equation (1.49) while the velocity of the surface recombination s_e and photogenerated charge Q_{00} were evaluated.

The velocity of the hole surface recombination, however, could not be evaluated from the collected charge, because it is also affected by the hole trapping. The charge that entered bulk (obtained by MC) was used for fitting instead. Obtained photogenerated charge and surface recombination velocity presented Table 3.2.

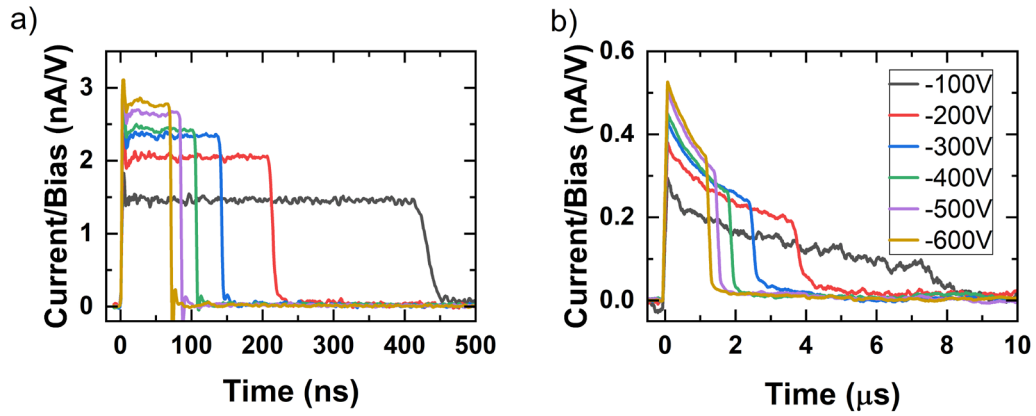

Fig. 3.5: Bias-normalized pulsed bias dependence of a) electron waveforms in FSe geometry and b) hole waveforms in GRSh geometry.

Table 3.2: Surface recombination velocity

	Electrons	Holes
Photogenerated charge Q_{00} (fC)	135	476
Velocity of the surface recombination s (cm. s^{-1})	5.14 $\times 10^5$	3.11×10^4

3.3.2 Measurement in the polarized detector

Waveforms in the DC bias regime (polarized detector) were acquired 10 minutes after the biasing. It is necessary to wait until the stabilization of the waveforms (DC steady-state) or until the waveform evolution is significantly slower than the data acquisition time. If not, the data would be distorted, since several thousands of consecutive current waveforms are averaged to increase signal-to-ratio. The electron and hole waveforms measured in the polarized detector are shown in Fig. 3.6 and

Fig. *3.7*, respectively. The MC fit is represented by the black dashed lines and the electric field profile obtained by MC is shown in the inset. The previously flat electron waveforms are now increasing in time (see Fig. 3.6) and hole waveforms in

Fig. *3.7* are now decreasing more rapidly (than in the unpolarized detector). Below the -200V formation of the inactive layer beneath the cathode can be seen – in the case of electrons (Fig. 3.6) no current waveforms can be seen and in the case of holes (

Fig. *3.7*) no apparent transit time is observed. The profile of the fitted electric field according to the Gauss's law corresponds to the negative space charge. Linear

electric field did not achieve the desired MC fit, so quadratic electric field was used as a next order Taylor series expansion of the electric field instead. The MC simulation below $-200V$ could not be evaluated unambiguously – either because there was no waveform or because there was no observable transit time, by which the effect of electric field and charge trapping could be distinguished. Carrier mobilities and the surface recombination velocities obtained in pulsed bias regime were used for DC regime fitting and only the electric field and the carrier lifetime were fitted in DC. The deep level trapping time fitted by MC simulation shows significant shortening compared to the unpolarized detector. The fitted electron lifetime remains still extremally high. The change of the hole trapping time will be later shown in laser pulse delay measurement together with the evolution of the space charge.

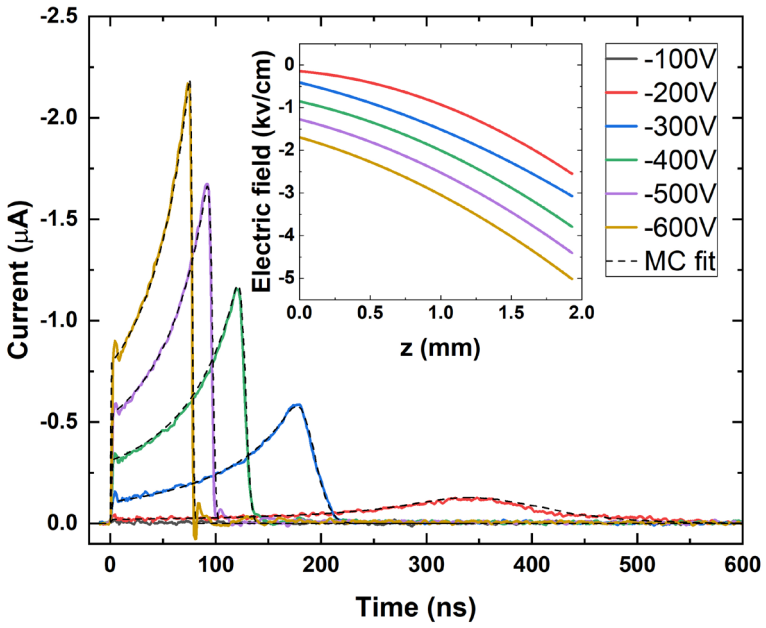

Fig. 3.6: DC bias dependence of the electron current waveforms in FSe geometry. Black dashed lines represent the fit by MC simulation. Electric field profile obtained by MC simulation is shown in the inset.

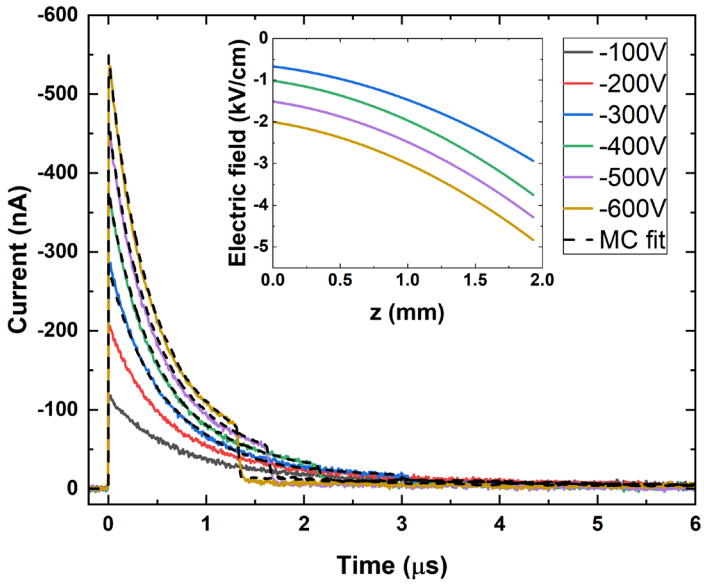

Fig. 3.7: DC bias dependence of the hole current waveforms in GRSh geometry. Black dashed lines represent the fit by MC simulation. Electric field profile obtained by MC simulation is shown in the inset.

The formation of the negative space charge can be explained either by the depletion of holes or injection of electrons. However, hole depletion is more probable since the material is p-type and data are measured in the reverse direction of Schottky contact. Another compliant argument is that the slope of the electric field is bigger beneath the anode than the cathode, which corresponds to more electrons being trapped beneath the anode $z = L$ than the cathode $z = 0$. If it was the effect of electron injection, the charge density would be uniform in the whole detector since extremely high electron lifetime was measured.

3.3.3 Dynamics of the space charge formation in the dark

Lastly, the temporal evolution of the detector polarization at -400V was measured by changing the LPD. Waveforms until the LPD $= 5$s were acquired in the pulsed bias regime, where one waveform per bias pulse was measured. Any larger LPDs were measured in DC bias regime, where the mean time of data averaging $\left(\frac{t_{start}+t_{end}}{2}\right)$ was used as a LPD.

The time evolution of electron and hole current waveforms depending on the laser pulse delay (LPD) are shown in Fig. 3.10 and Fig. 3.9, respectively. Black dashed

lines represent the fit by MC simulation and the electric field profile obtained by MC simulation for each bias is shown in the inset.

The time evolution (LPD) of electron waveforms Fig. 3.8 shows gradual twisting of the waveforms attributable to the negative space charge build-up. The same goes for the hole waveforms in Fig. 3.9. The electric field profile in the insets is at first linear but as the time progresses (LPD) the quadratic term appears. No noticeable change of electric field was observed until LPD $= 1\text{ms}$ and the evolution of the electric field saturates at LPD $= 1\text{h}$.

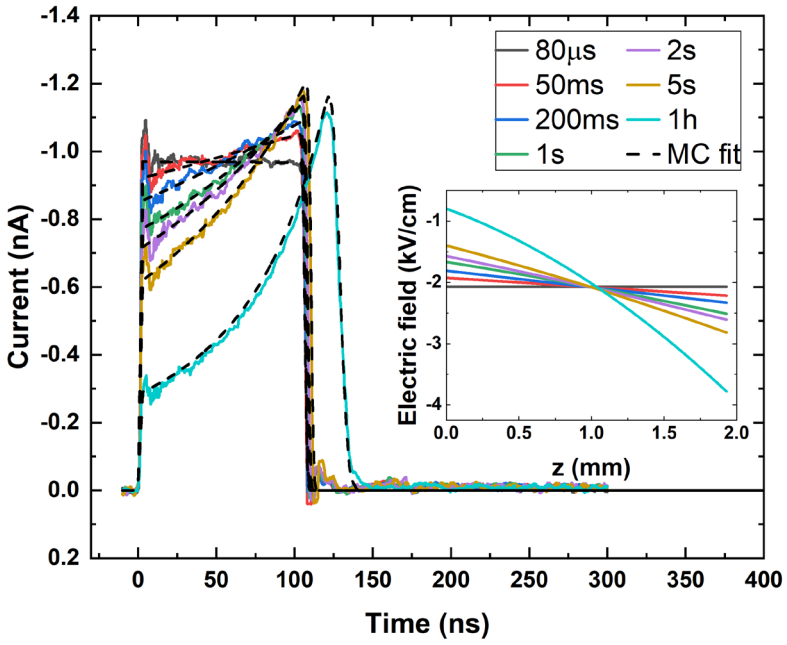

Fig. 3.8: Temporal (LPD) evolution of the electron current waveforms measured at $U = -400V$. Black dashed lines represent the fit by MC simulation. Electric field profile obtained by MC simulation (dashed) is shown in the inset.

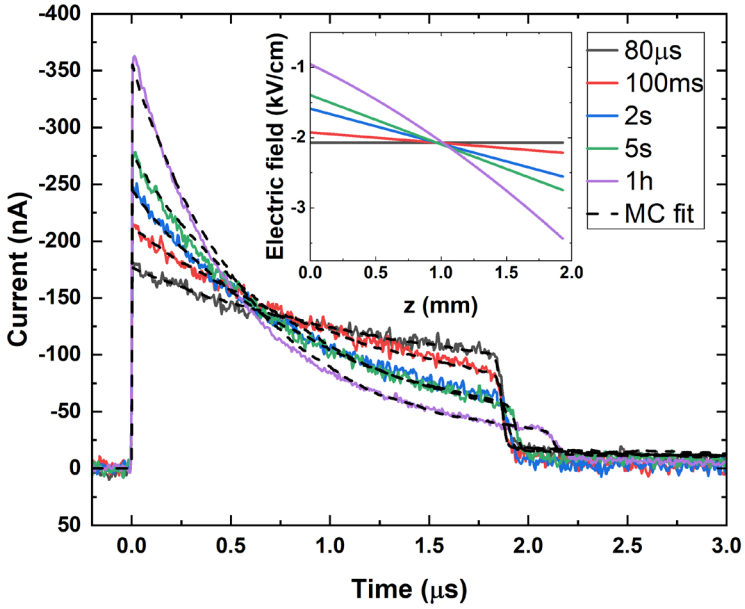

Fig. 3.9: Temporal (LPD) evolution of the hole current waveforms measured at $U = -400V$. Black dashed lines represent the fit by MC simulation. Electric field profile obtained by MC simulation (dashed) is shown in the inset.

Using the MC simulation was found that the electron lifetime is not affected by the space charge but the lifetime of holes changes significantly. The average charge density dependence on the LPD is shown in Fig. 3.10 a). The dependence of the hole deep-level trapping rate (inverse of trapping time) is shown in Fig. 3.10 b). The trapping rate undoubtedly rises with increasing space charge and one can assume that the trap responsible for the detector polarization is a hole recombination centre. If the trap causing the detector polarization is the same as the trap responsible for hole trapping, then the trapping rate is governed by the formula (1.27) and therefore the hole trapping rate should be linearly dependent of space charge (concentration of the occupied trap states). Since it is not the case, there must be another (deep hole) trap with different capture cross-section – the trap with shorter trapping time will fill faster than the trap with longer trapping time.

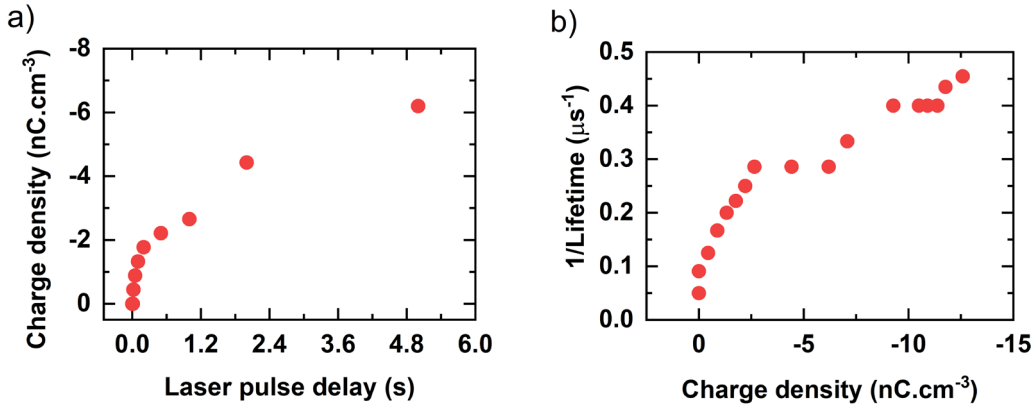

Fig. 3.10: a) Temporal (LPD) evolution of the average charge density. b) Dependence of the trapping rate on the average charge density.

3.3.4 The CCE in the dark

Knowing the photogenerated Q_{00} and collected charge of electrons and holes, the charge collection efficiency was evaluated. The electron CCE is affected only by carrier recombination and therefore was fitted by (1.49). The hole CCE was fitted by the modified single carrier Hecht relation (1.51). Evaluated CCEs are shown in Fig. 3.11. The hole CCE in polarized DC bias regime is a result of a competition of the lowering of the hole surface recombination and increasing deep-level trapping rate. The electric field beneath the anode is increasing due to the negative space charge thanks to what the hole surface recombination is suppressed on the other side the presence of the negative space charge increases the deep-level trapping rate. Eventually, both contributions to CCE partially cancel out.

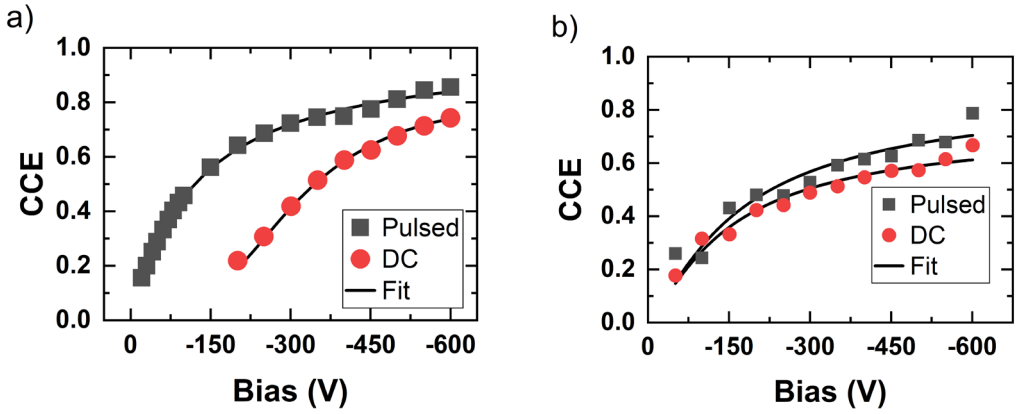

Fig. 3.11: Dependence of the a) electron and b) hole collection efficiency on the applied bias in pulsed and DC bias regime. Black lines represent fit by in a) equation (1.49) and in b) by modified single carrier Hecht equation (1.51).

The temporal evolution of the charge collection efficiency is presented in Fig. 3.12. The CCE is decreasing in both cases with LPD. In the case of electrons, the decrease of the CCE is tied with the decrease of the electric field beneath the cathode and concurrently amplifying the surface recombination. Collection efficiency of holes is mainly decreasing due to the measured degradation of the hole lifetime as the negative space charge builds up. The overshoots in CCE are likely caused by the decrease of the surface recombination but the exact process is not yet clear and will be studied more thoroughly in further research.

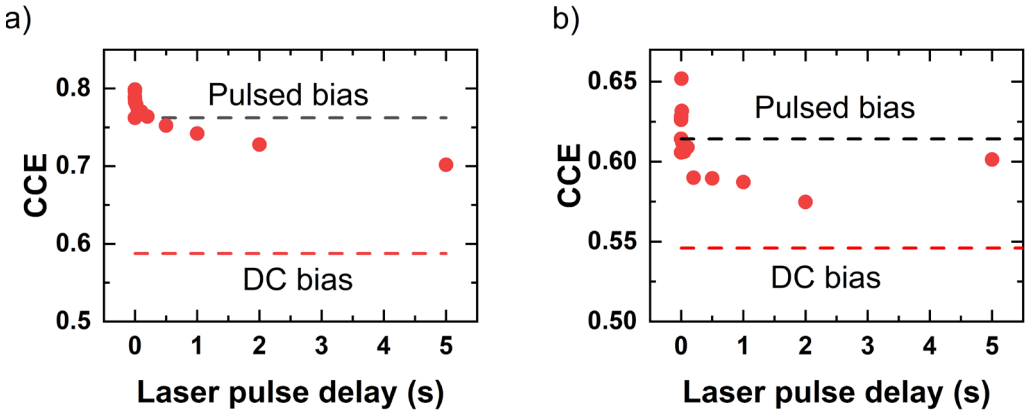

Fig. 3.12: Temporal evolution (dark) of the a) electron and b) hole collection efficiency. Dashed lines represent the limit values of CCE measured in pulsed and DC bias regime with the same voltage applied.

3.4 Continuous anode illumination

Firstly, the LED intensity dependence of waveforms was measured in DC bias regime at -400V. Data averaging and detector illumination started only after the biased detector reached quasi-steady-state (concluded by the current waveforms). After the measurement was over the bias and LED was turned off allowing the detector to depolarize and then measurement with different intensity started over. As a result the electron Fig. 3.13 and hole Fig. 3.14 waveforms were obtained. The LED intensity is in the figures below displayed as the density of the LED induced photocurrent. The photocurrent was chosen due to the fact, that the LED and the sample detector had to be removed in order to switch the measurement geometry (FSe, GRSh) or side of the LED illumination. After the setup adjustment, the LED could not be aligned perfectly with its previous position, therefore a slightly different photocurrent was measured for the same LED intensity (more in section 2).

As seen in the insets of the electric field profile in Fig. 3.13 and Fig. 3.14, with the increasing photocurrent, the electric field beneath the cathode also rises and beneath anode decreases. This twisting of the electric field is a result of mitigating the negative space charge, which for the photocurrent density above - 142nA. cm^{-2} even changes sign. The completely flat electron waveform (also has shortest transit time) shown green in Fig. 3.13 has the same transit time as the waveform measured at -400V in the unpolarized detector. This suggests that the electric field is for this respective photocurrent indeed constant. A similar effect was measured for holes at -336nA. cm^{-2} almost constant electric field and deep level trapping time (25μs) similar to that in the unpolarized detector (20μs) was obtained by the MC simulation.

For higher photocurrent than -142nA. cm^{-2} (positive space charge) the shortening of electron lifetime was observed in Fig. 3.15 b) (grey square). The lifetime of holes beyond -336nA. cm^{-2} practically does not change as can be seen in Fig. 3.15 b) (red point). The dependence of the charge density on the density of the photocurrent in Fig. 3.14 a) is roughly the same for both FSe and GRSh geometries, which suggests that the LED was returned to a similar position relative to the detector and the mask.

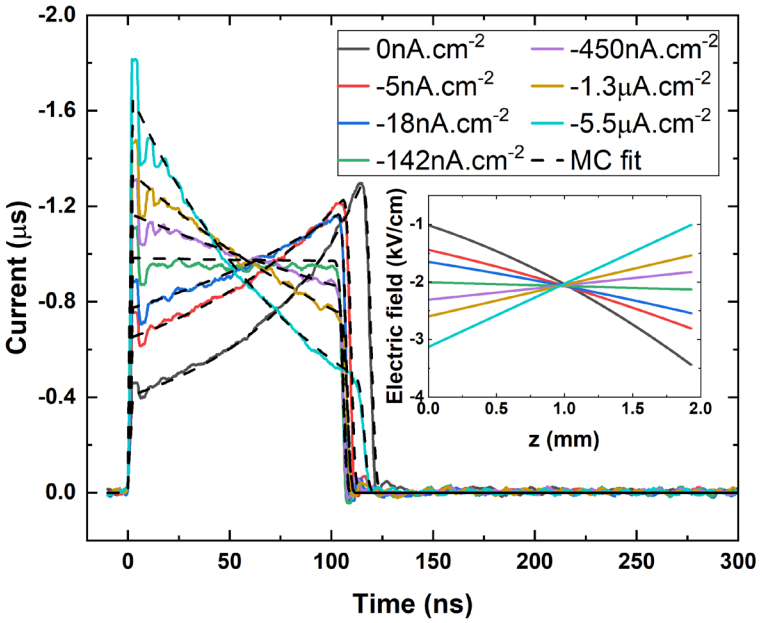

Fig. 3.13: LED intensity dependence (illuminated anode) of the electron waveforms measured in FSe geometry. Black dashed lines represent the fit by MC simulation. Electric field profile obtained by MC simulation (dashed) is shown in the inset.

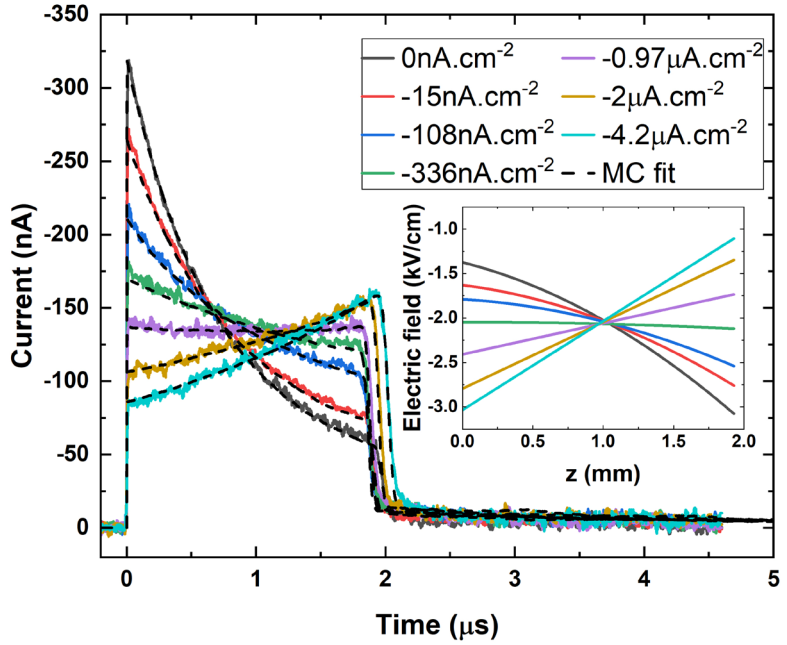

Fig. 3.14: LED intensity dependence (illuminated anode) of the hole waveforms measured in GRSh geometry. Black dashed lines represent the fit by MC simulation. Electric field profile obtained by MC simulation (dashed) is shown in the inset.

In Fig. 3.15 c) and d) the dependence of electron and hole trapping rate is shown. The trapping rate of electrons is linearly dependent on average charge density (for positive charge density). The disruption of linear behaviour is caused mostly by the MC fitting. For negative charge densities, no trapping of electrons was assumed to simplify the fitting process and for charge density close to zero, the transit time does not strongly depend on charge density thus a relatively wide range of trapping times satisfies the fit. Using the same thought process as in the dark measurement, the linear increase of trapping rate with charge density means that one trap is responsible for positive space charge build-up and the increase of trapping rate of electrons.

In the case of trapping rate of holes it is hard to describe the dependence since in the area of interest the data are most affected by the fitting error. But if we look only at negative charge densities, the dependence is not linear which corresponds to the measurement in the dark.

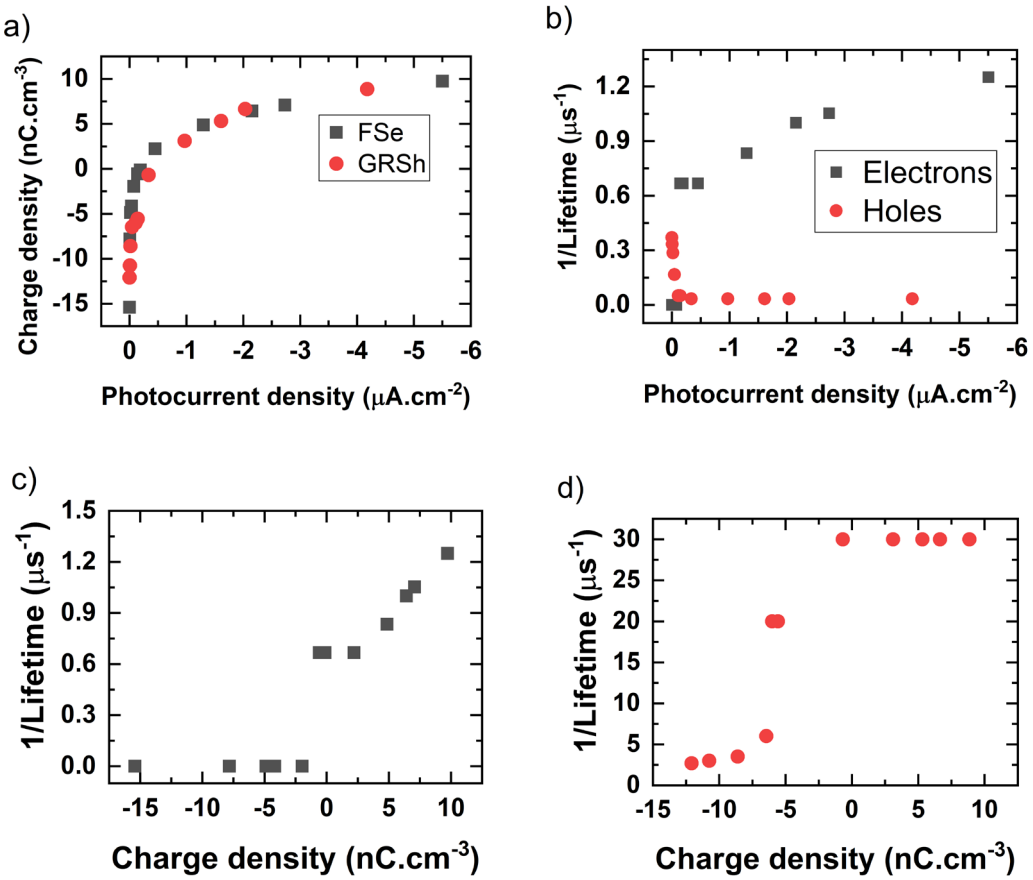

Fig. 3.15: a) Dependence of the average charge density on the LED induced photocurrent. b) Dependence of the trapping rate on the LED induced photocurrent. c) Dependence of the electron trapping rate on the average charge density. d) Dependence of the hole trapping rate on the average charge density.

The CCE for the measurements above is shown in Fig. 3.16. The electron CCE rises together with electric field beneath the cathode until the point the surface recombination is completely suppressed and then saturates. The effect of the shortening of the electron lifetime is not seen, as it is hidden in the saturation of the surface recombination. The CCE of holes starts from its (dark) DC bias regime limit, then reaches a maximum and starts to decrease below the DC limit. We assume that the maximum is formed by the competition of increasing hole surface recombination and decreasing hole trapping rate. The maximum is located in the region, where the trapping rate of holes becomes constant, from this point on the surface recombination takes over and CCE starts to fall.

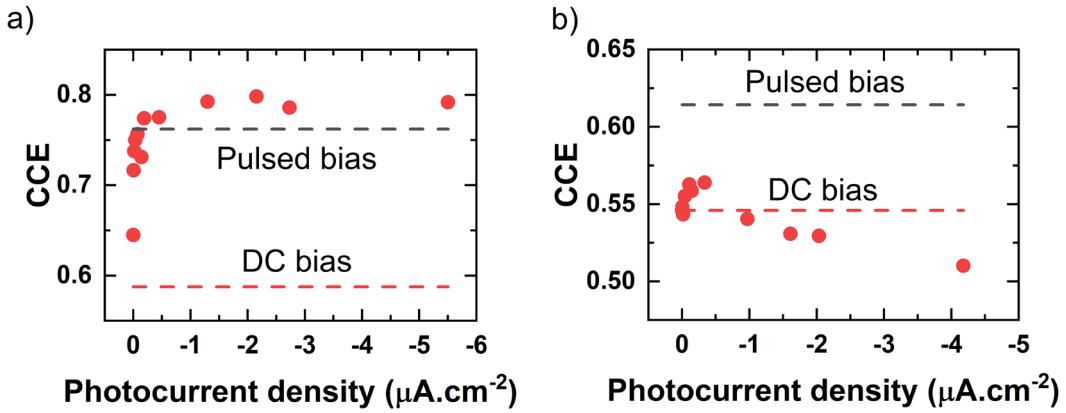

Fig. 3.16: Dependence of a) electron and b) hole CCE on the density of the LED induced photocurrent (illuminated anode)

As was discussed in the previous section, the inactive layer is formed in the DC bias regime and since anode illumination suppresses the detector polarization, the flat-electric field bias dependence was also measured. After the DC biasing and the waveform stabilizing, such LED intensity was set that the measured waveforms were flat. Fig. 3.17 clearly demonstrates that the LED anode illumination is able to repress the inactive layer after it is formed. The LED induced photocurrent density required to flatten the electric field is in the inset compared to the dark current. On average the photocurrent needs to be 6.6 times the dark current in order to obtain flat electron waveforms.

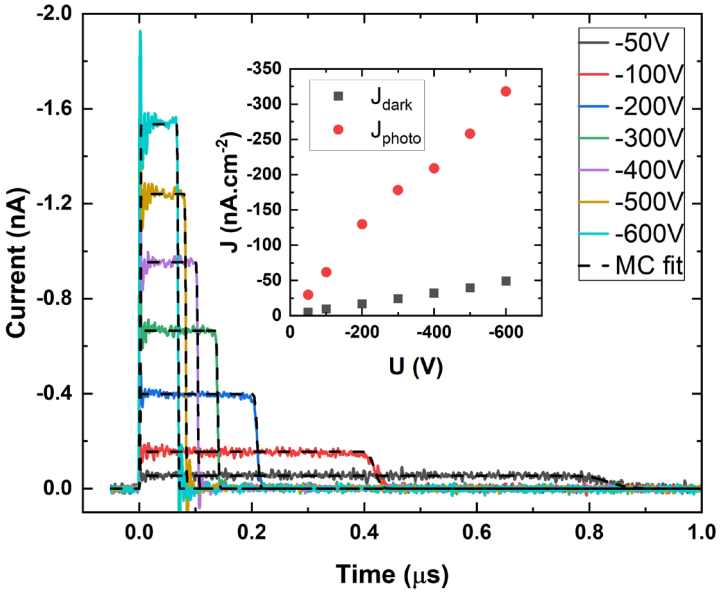

Fig. 3.17: Flat electric field (continuous LED anode illumination) DC bias dependence of the current waveforms. Black dashed lines represent the fit by MC simulation. Corresponding photocurrent density is compared to the dark current density in the inset.

3.5 Continuous cathode illumination

Lastly, the illumination of the cathode was studied. The dependence on LED intensity (induced photocurrent) was measured the same way as for the case of the illuminated anode. The measured electron and hole signals are shown in Fig. 3.18 and Fig. 3.19 respectively. For better clarity, only the waveforms with visible change are shown in both figures. This time the illumination induced change was not as significant as for the anode illumination even though the induced photocurrent was twice that high. Right after the biased-detector illumination, the electron waveforms shortened and as the measured dependence displays, the higher the LED intensity the more noticeable the change. But for high intensities this effect saturates. The shortening of the waveforms can only be explained by the partial suppression of the negative space charge since the transit time in the depolarized detector was identical before and after the illumination. The already built up negative space charge was probably compensated by the holes that were sucked in from the anode. A decrease of the deep hole trap was observed from 3µs in the dark to 2µs under the maximal illumination.

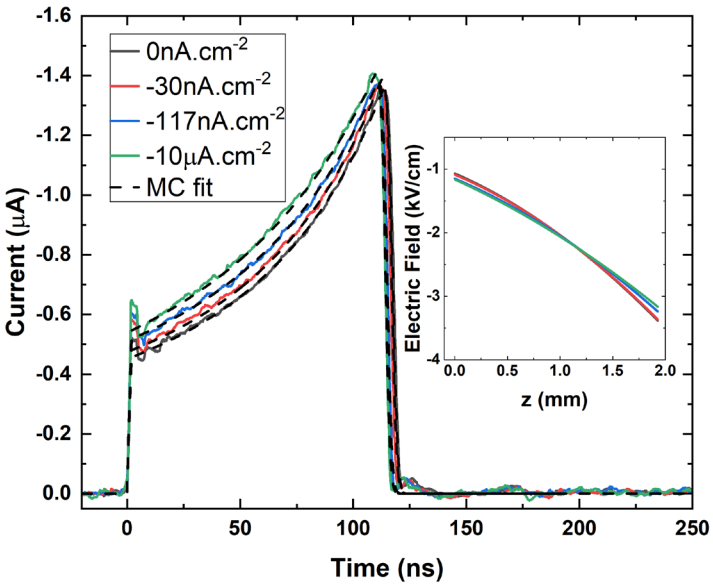

Fig. 3.18: LED intensity dependence (illuminated cathode) of the electron current waveforms measured in FSe geometry. Black dashed lines represent the fit by MC simulation. Electric field profile obtained by MC simulation (dashed) is shown in the inset.

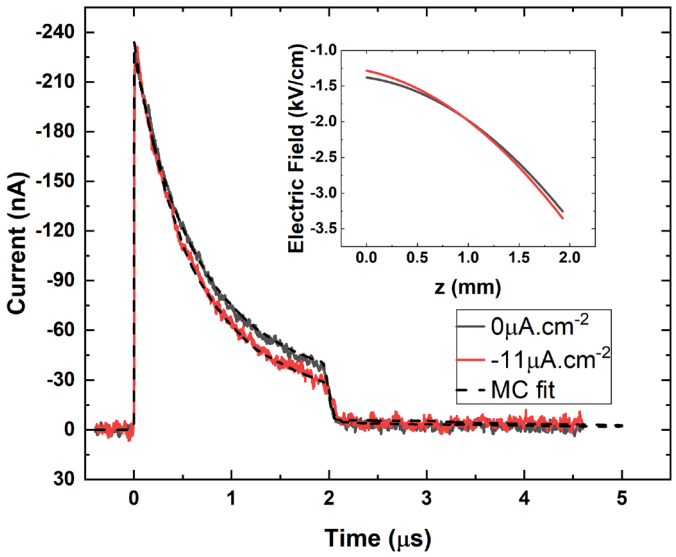

Fig. 3.19: LED intensity dependence (illuminated cathode) of the hole current waveforms measured in GRSh geometry. Black dashed lines represent the fit by MC simulation. Electric field profile obtained by MC simulation (dashed) is shown in the inset.

Due to the injection of additional electrons, the electron surface recombination is lowering with increasing intensity, which combined with a small decline of the space charge results in the slow saturation of the electron CCE as can be seen in Fig. 3.20 a). The gradual decline of the hole CCE in Fig. 3.20 b) can be attributed to increased trapping rate of holes.

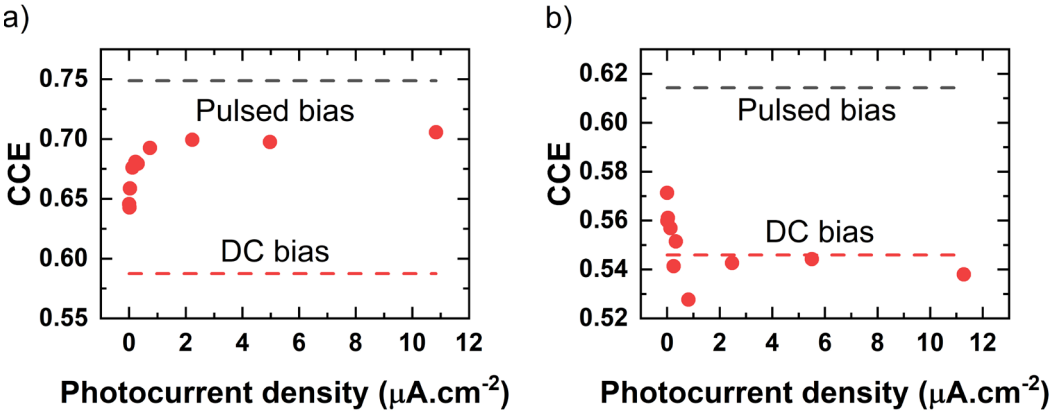

Fig. 3.20 a) Electron and b) hole collection efficiency in a detector with LED illuminated cathode.

4 Conclusion

In this thesis, the detector transport properties were evaluated in the dark and under continuous LED illumination using the Laser-induced Transient Current Technique and in-house made Monte Carlo simulation for fitting the measured current waveforms. In the dark, the electron and hole signals were measured in the unpolarized and polarized detector. The electron and hole mobility of $\mu_e = 950\ \mathrm{cm}^2.\mathrm{V}^{-1}.\mathrm{s}^{-1}$ and $\mu_h = 50\mathrm{cm}^2.\mathrm{V}^{-1}.\mathrm{s}^{-1}$ respectively were determined from the unpolarized current waveforms. The hole waveforms were fitted by a two-level system of one shallow and one deep hole trap and the hole lifetime of $11\mu\mathrm{s}$ was found. The electron lifetime, however, could not be successfully evaluated as for the -20V no decay of the electron current waveforms was observed. In the DC bias regime, the current waveforms were strongly affected by the presence of the negative space charge in the detector. Presence of this space charge visibly reduced the hole lifetime and corresponding charge collection efficiency. The electron collection efficiency in the dark detector was only affected by the surface recombination.

The continuous illumination of the anode led to an increase in charge collection efficiency of both types of carries until the surface recombination took over and decrease the CCE of holes. It was also found out that the anode illumination is able to compensate built-up space charge, change its sign or even eliminate the already formed inactive layer.

The effect of the illumination of the cathode was much less prominent. The partial compensation of negative space charge by injected holes was observed. The exact mechanism of holes injection is not yet understood and will be subjected to follow-up research.

The negative space charge formation after the biasing, its compensating by the anode illumination and almost no effect of cathode illumination all point to the fact, that the detector biased in FSe and GRSh geometry polarizes due to the hole depletion. Therefore, the anode illumination provides the holes that would otherwise be blocked by the Schottky contact resulting in suppression of negative space charge formation. The cathode illumination provides additional electrons but due to their exceptionally high lifetime, their effect is negligible.

Since it was found out that the continuous illumination sufficiently suppresses the detector polarization only the continuous LED illumination was measured. The additional illumination by the LED pulses will be the object of our next study.

5 Bibliography

[1] T. E. Schlesinger and R. B. James, *Semiconductors for room temperature nuclear detector applications*. San Diego: Academic Press, 1995.

[2] P. Guerra, D. G. Darambara, D. Visvikis, and A. Santos, "Optimization of a pixellated CdZnTe/CdTe detector for a multi-modality imaging system," in *2007 IEEE Nuclear Science Symposium Conference Record*, Honolulu, HI, USA, 2007, pp. 2976–2979, doi: 10.1109/NSSMIC.2007.4436759.

[3] A. I. Ayzenshtat *et al.*, "GaAs as a material for particle detectors," *Nucl. Instrum. Methods Phys. Res. Sect. Accel. Spectrometers Detect. Assoc. Equip.*, vol. 494, no. 1, pp. 120–127, Nov. 2002, doi: 10.1016/S0168-9002(02)01455-9.

[4] D. Vartsky *et al.*, "Radiation induced polarization in CdTe detectors," *Nucl. Instrum. Methods Phys. Res. Sect. Accel. Spectrometers Detect. Assoc. Equip.*, vol. 263, no. 2, pp. 457–462, Jan. 1988, doi: 10.1016/0168-9002(88)90986-2.

[5] A. Cola and I. Farella, "The polarization mechanism in CdTe Schottky detectors," *Appl. Phys. Lett.*, vol. 94, no. 10, p. 102113, Mar. 2009, doi: 10.1063/1.3099051.

[6] J. Franc and P. Höschl, "Fyzika polovodičů pro Optoelektroniku I." 2014.

[7] R. P. Feynman, R. B. Leighton, and M. Sands, "4-6 Gauss' law; the divergence of E," in *The Feynman Lectures on Physics Volume II*, New Millenium Edition., Basic Books, 2011.

[8] W. Shockley, "Currents to Conductors Induced by a Moving Point Charge," *J. Appl. Phys.*, vol. 9, no. 10, pp. 635–636, Oct. 1938, doi: 10.1063/1.1710367.

[9] R. Grill *et al.*, "Polarization Study of Defect Structure of CdTe Radiation Detectors," *IEEE Trans. Nucl. Sci.*, vol. 58, no. 6, pp. 3172–3181, Dec. 2011, doi: 10.1109/TNS.2011.2165730.

[10] W. Shockley and W. T. Read, "Statistics of the Recombinations of Holes and Electrons," *Phys. Rev.*, vol. 87, no. 5, pp. 835–842, Sep. 1952, doi: 10.1103/PhysRev.87.835.

[11] L. Reggiani, *Hot-Electron Transport in Semiconductors*. Springer Berlin Heidelberg, 1985.

[12] W. E. Tefft, "Trapping Effects in Drift Mobility Experiments," *J. Appl. Phys.*, vol. 38, no. 13, pp. 5265–5272, Dec. 1967, doi: 10.1063/1.1709312.

[13] K. Suzuki, M. Shorohov, T. Sawada, and S. Seto, "Time-of-Flight Measurements on TlBr Detectors," *IEEE Trans. Nucl. Sci.*, vol. 62, no. 2, pp. 433–436, Apr. 2015, doi: 10.1109/TNS.2015.2403279.

[14] A. Levi, M. M. Schieber, and Z. Burshtein, "Carrier surface recombination in HgI_2 photon detectors," *J. Appl. Phys.*, vol. 54, no. 5, pp. 2472–2476, May 1983, doi: 10.1063/1.332363.

[15] K. Suzuki and H. Shiraki, "Evaluation of surface recombination velocity of CdTe radiation detectors by time-of-flight measurements," in *2008 IEEE Nuclear Science Symposium Conference Record*, Oct. 2008, pp. 213–216, doi: 10.1109/NSSMIC.2008.4775165.

[16] K. Hecht, "Zum Mechanismus des lichtelektrischen Primärstromes in isolierenden Kristallen," *Z. Für Phys.*, vol. 77, no. 3, pp. 235–245, Mar. 1932, doi: 10.1007/BF01338917.

[17] Š. Uxa, E. Belas, R. Grill, P. Praus, and R. B. James, "Determination of Electric-Field Profile in CdTe and CdZnTe Detectors Using Transient-Current Technique," *IEEE Trans. Nucl. Sci.*, vol. 59, no. 5, pp. 2402–2408, Oct. 2012, doi: 10.1109/TNS.2012.2211615.

[18] K. Suzuki, T. Sawada, and K. Imai, "Effect of DC Bias Field on the Time-of-Flight Current Waveforms of CdTe and CdZnTe Detectors," *IEEE Trans. Nucl. Sci.*, vol. 58, no. 4, pp. 1958–1963, Aug. 2011, doi: 10.1109/TNS.2011.2138719.

[19] J. Fink, H. Krüger, P. Lodomez, and N. Wermes, "Characterization of charge collection in CdTe and CZT using the transient current technique," *Nucl. Instrum.*

Methods Phys. Res. Sect. Accel. Spectrometers Detect. Assoc. Equip., vol. 560, no. 2, pp. 435–443, May 2006, doi: 10.1016/j.nima.2006.01.072.
[20] J. Pipek, "Charge transport in semiconducting radiation detectors," Charles University, 2018.
[21] P. Praus, E. Belas, J. Bok, R. Grill, and J. Pekárek, "Laser Induced Transient Current Pulse Shape Formation in (CdZn)Te Detectors," *IEEE Trans. Nucl. Sci.*, vol. 63, no. 1, pp. 246–251, Feb. 2016, doi: 10.1109/TNS.2015.2503600.
[22] C. Jacoboni and L. Reggiani, "The Monte Carlo method for the solution of charge transport in semiconductors with applications to covalent materials," *Rev. Mod. Phys.*, vol. 55, no. 3, pp. 645–705, Jul. 1983, doi: 10.1103/RevModPhys.55.645.
[23] A. V. Tyazhev, V. Novikov, O. Tolbanov, A. Zarubin, M. Fiederle, and E. Hamann, "Investigation of the current-voltage characteristics, the electric field distribution and the charge collection efficiency in X-ray sensors based on chromium compensated gallium arsenide," Sep. 2014, vol. 9213, p. 92130G, doi: 10.1117/12.2061302.

6 List of Figures

Fig. 1.1: Simplified geometry of the detector. 6
Fig. 1.2: Normalized current waveforms for different biases. Waveforms are normalized with respect to the current I_0 and trasit time t_{r0} of the U_0 waveform. 9
Fig. 1.3: a) Normalized electric field profile for different values of charge density ρ and b) corresponding profile of the normalized charge density. 10
Fig. 1.4: a) Broadening $\rho < 0$ and b) shortening $\rho > 0$ of the carrier distribution due to the non-constant electric field. 11
Fig. 1.5: Normalized current waveforms calculated for different space charge distributions $\rho(z)$. 12
Fig. 1.6: Band diagram of the possible defect described by the Shockley-Read-Hall model. 13
Fig. 1.7: Normalized current waveforms a) for different trapping times τ_t and no detrapping (deep trap) and b) for $\tau_t = t_r$ and different de-trapping times τ_d (shallow trap). 15
Fig. 1.8: a) Comparison of the first-order approximation with the precise analytical solution (1.45) for different average trapping and b) convergence of the higher-order approximations. 17
Fig. 1.9: a) Normalized current waveform with different (de-) trapping and b) increase of the transit time t_r due to the effective mobility 18
Fig. 1.10: Current waveforms normalized by bias for the model a) without surface recombination and b) with surface recombination 19
Fig. 2.1: Scheme of our L-TCT setup 21
Fig. 2.2: Masking of the detector 22
Fig. 2.3: Relative position of bias and laser pulse [20] 23
Fig. 2.4: Experimental setup configuration of the measurement of the electron and hole signals. 24
Fig. 3.1: Physical dimensions of the detector 26
Fig. 3.2: Current-voltage characteristic. Bias was applied to the full electrode side (FS). Inset shows detail of the I-V characteristics with negative polarity 27
Fig. 3.3: Pulsed bias dependence of electron current waveforms in FSe geometry 29
Fig. 3.4: Pulsed bias dependence of the hole current waveforms in GRSh geometry 29

Fig. 3.5: Bias-normalized pulsed bias dependence of a) electron waveforms in FSe geometry and b) hole waveforms in GRSh geometry. 31
Fig. 3.6: DC bias dependence of the electron current waveforms. 32
Fig. 3.7: DC bias dependence of the hole current waveforms. 33
Fig. 3.8: Temporal evolution of the electron current waveforms 34
Fig. 3.9: Temporal evolution of the hole current waveforms 35
Fig. 3.10: a) Temporal evolution of the average charge density. b) Dependence of the trapping rate on the average charge density. 36
Fig. 3.11: Dependence of the a) electron and b) hole collection efficiency on the applied bias in pulsed and DC bias regime. 36
Fig. 3.12: Temporal evolution of the a) electron and b) hole collection efficiency... 37
Fig. 3.13: LED intensity dependence (illuminated anode) of the electron waveforms measured in FSe geometry.. 39
Fig. 3.14: LED intensity dependence (illuminated anode) of the hole waveforms measured in GRSh geometry. 39
Fig. 3.15: a) Dependence of the average charge density on the LED induced photocurrent. b) Dependence of the trapping rate on the LED induced photocurrent. c) Dependence of the electron trapping rate on the average charge density. d) Dependence of the hole trapping rate on the average charge density. 40
Fig. 3.16: Dependence of a) electron and b) hole CCE on the density of the LED induced photocurrent (illuminated anode) 41
Fig. 3.17: Flat electric field (continuous LED anode illumination) DC bias dependence of the current waveforms 42
Fig. 3.18: LED intensity dependence (illuminated cathode) of the electron current waveforms measured in FSe geometry. 43
Fig. 3.19: LED intensity dependence (illuminated cathode) of the hole current waveforms measured in GRSh geometry 43
Fig. 3.20 a) Electron and b) hole collection efficiency in a detector with LED illuminated cathode. 44

7 List of Tables

Table 0.1: Selected properties of Si, Ge, CdZnTe and GaAs 4

Table 3.1: Transport properties of the unpolarized detector obtained by MC simulation 30

Table 3.2: Surface recombination velocity 31

8 List of Symbols and Abbreviations

α	absorption coefficient
BPW	bias pulse width
$\delta(z)$	Dirac delta function
CCE	charge collection efficiency (definition in section 1.5)
D_e, D_h	electron and hole diffusion coefficient
DT	depolarization time
e	elementary charge
ε	permittivity of the material
$E(z,t)$	electric field
$E_0(z,t)$	applied electric field
E_g	with of the bandgap
$E_\rho(z,t)$	electric field exerted by the charge density ρ
E_t	the energy of the trapping centre in the bandgap
FS	full electrode side of the detector
FSe, FSh	measurement of electron and hole signal from FS (more in Fig. 2.4)
GR	guard ring
GRS	guard ring side of the detector
$GRSe, GRSh$	measurement of electron and hole signal form GRS (more in Fig. 2.4)
$\chi(t,t_1,t_2)$	boxcar function, $\chi(t,t_1,t_2)=1$ for $t_1 \leq t \leq t_2$ else $\chi(t,t_1,t_2)=0$
$I(t)$	the electric current measured as a current waveform
$J_1(z)$	modified Bessel function of the first kind of order one
j_e, j_h	electron and hole current density
k_B	Boltzmann constant
L	width of the detector
$L-TCT$	Laser-induced Transient Current Technique
LPD	laser pulse delay (relative to the rising edge of the bias pulse)
MC	Monte Carlo simulation
μ_e, μ_h	electron and hole mobility
μ_{eff}	effective mobility
$n(z,t)$	the density of free electrons in the conduction band
n_0, n_0^0, n_0^k	the concentration of the free electrons, never trapped electrons and k-times detrapped electrons

n_1, n_1^k	the concentration of the trapped electrons and k-times trapped electrons
$N(t)$	number of trapping events until time t
N_0	number of photogenerated carriers (accounted for surface recombination)
N_{t0}, N_t	the concentration of the trapping centre, the concentration of occupied trap states
N_C, N_V	effective density of states in the conduction and the valence band
$p(z,t)$	density of free holes in valence band
PP	bias/ laser pulsing period
Q_0	photogenerated charge (accounted for surface recombination)
Q_{00}	photogenerated charge (without surface recombination)
ρ	charge density in the detector
ρ_m	charge density (definition in section 1.2.2)
S	area of the laser spot for L-TCT probing
s, s_e, s_h	the velocity of the surface recombination, velocity of electron and hole surface recombination
S_e, S_h	electron and hole Soret coefficient coefficient
σ_n, σ_p	electron and hole capture cross-section of the trapping centre
T	absolute temperature of the sample
$\tau_d, \tau_d^n, \tau_d^p$	detrapping time, electron detrapping time, hole detrapping time
$\theta(z)$	Heaviside theta function, $\theta(z) = 0$ for $z \leq 0$, $\theta(z) = 1$ for $z > 0$
t_{laser}	with of the L-TCT probing laser pulse
t_{r0}, t_r	default transit time (constant electric field), transit time
$t_{r\ 1/2}$	the time required for carriers to travel half of the width of the detector
$\tau_t, \tau_t^n, \tau_t^p$	trapping time, electron trapping time, hole trapping time
U	applied bias
v_0	drift velocity in constant electric field
$v_e(z)$	arbitrary electron drift velocity
v_{th}^n, v_{th}^p	the thermal velocity of the electrons and holes